Modeling buckling and topological defects in stacked two-dimensional layers of graphene and hexagonal boron nitride

K. R. Elder, C. V. Achim, V. Heinonen, E. Granato, S. C. Ying, and T. Ala-Nissila

Phys. Rev. Materials **5**, 034004 — Published 12 March 2021

DOI: 10.1103/PhysRevMaterials.5.034004

Modeling buckling and topological defects in stacked two dimensional layers of graphene and hexagonal boron nitride.

K. R. Elder,[1] C. V. Achim,[2] V. Heinonen,[3] E. Granato,[4, 5] S.C. Ying,[5] and T. Ala-Nissila[2, 5, 6]
[1]*Department of Physics, Oakland University, Rochester, Michigan 48309, USA*
[2]*QTF Centre of Excellence, Department of Applied Physics,*
Aalto University School of Science, P.O. Box 11000, FI-00076 Aalto, Espoo, Finland
[3]*Department of Mathematics, Massachusetts Institute of Technology,*
77 Massachusetts Avenue, Cambridge, Massachusetts 02139-4307, USA
[4]*Laboratório Associado de Sensores e Materiais,*
Instituto Nacional de Pesquisas Espaciais,12227-010 São José dos Campos, SP, Brazil
[5]*Department of Physics, P.O. Box 1843, Brown University, Providence, RI 02912-1843, USA*
[6]*Interdisciplinary Centre for Mathematical Modelling,*
Department of Mathematical Sciences, Loughborough University,
Loughborough, Leicestershire LE11 3TU, UK
(Dated: February 26, 2021)

In this paper a two dimensional phase field crystal model of graphene and hexagonal boron nitride (hBN) is extended to include out of plane deformations in stacked multi-layer systems. As proof of principle the model is shown analytically to reduce to standard models of flexible sheets in the small deformation limit. Applications to strained sheets, dislocation dipoles and grain boundaries are used to validate the behavior of a single flexible graphene layer. For the multi-layer systems, parameters are obtained to match existing theoretical density functional theory calculations for graphene/graphene, hBN/hBN and graphene/hBN bilayers. More precisely it is shown that the parameters can be chosen to closely match the stacking energies and layer spacing calculated by Zhou *et al.* [1]. Further validation of the model is presented in a study of rotated graphene bilayers and stacking boundaries. The flexibility of the model is illustrated by simulations that highlight the impact of a complex microstructures in one layer on the other layer in a graphene/graphene bilayer.

I. INTRODUCTION

The properties of materials that can exist as stable two-dimensional (2D) layers and stacks of such layers has been of great interest due to their unusual properties and possible technological applications [2, 3]. Much of the initial interest has focused on graphene, but has now been extended to other interesting systems such as hexagonal boron nitride (hBN) and various transition metal dichalcogenides (TMDs) including MoS_2, $MoSe_2$ and WSe_2. Example applications include photodetectors [4, 5], catalysis [6] and solar energy absorption [7]. One difficulty in using these materials is the ability to grow large defect-free structures as it is well known that topological defects (dislocations, grain boundaries, domain-wall solitons and triple junctions) or phase interfaces can strongly impact electronic, mechanical, thermal and other properties in three dimensional (3D) materials. For example, in polycrystals the magnetic coercivity [8–11] and yield strength [12–17] vary by many orders of magnitude with changes in the average grain size. Naturally, similar changes in material properties can occur in 2D materials as has been observed in the thermal conductivity of graphene [18–20] and hBN [21] and in the electronic properties of TMDs [22, 23]

The purpose of this work is to develop a computational efficient method for studying the mechanical properties of such 2D materials and stacks of them using the phase field crystal (PFC) approach. The model presented incorporates out of plane deformations of each individual layer, coupling between the layers and elastic and plastic deformations within each plane. For this purpose the PFC approach [24–26] is used as it has already been developed for in-plane graphene [27] and hBN [28, 29] models and has been used to study defected structures such as grain boundaries, triple junctions and polycrystals. These prior publications provide extensive evidence that the models reproduce various experimental and numerical results such as the structure of dislocations and the non-monotomic change in grain boundaries with misorientation [27, 30, 31]. While atomistic methods such as molecular dynamics (MD) and density functional theory (DFT) can give great insights into such systems, it is extremely difficult to use them on the time and length scales relevant for many phenomena. It possible to exploit PFC type models as initial conditions for MD and DFT calculations to significantly reduce relaxation times. Such an approach has been used for MD studies of thermal conductivity in graphene and hBN [18–21] and MD and DFT studies of grain boundaries, triple junctions and polycrystals in graphene [27, 32, 33]. However, compared to atomistic approaches the PFC modeling can address much larger length and time scales.

In order to incorporate out-of-plane deformation in 2D PFC models another field, the height ($h(x, y)$), will be introduced to account for small out-of-plane deformations. In this work the Monge gauge is assumed, i.e., h is a single-valued function. This is in contrast to more sophisticated finite-element methods that allow for more complex three-dimensional shapes as in for example, the modeling of phase separation in multicomponent lipid bilayers [34, 35] and more relevantly in the PFC model for deformable spheres [36, 37]. While the use of a single-valued h field does limit the applicability of the model, it reduces the mathematical complexity and correspondingly increases the computational speed. As will be shown in Sec. II the mathematical form of the model is such that Fourier methods can be used which enhances the speed of calculations. To validate the model, it is shown analytically to reduce to traditional continuum models used to study flexible sheets [38, 39] and graphene [40] in the small deformation limit. Furthermore, in the numerical studies of strained sheets, 5/7 dislocation dipoles and grain boundaries are shown to reproduce analytic results and MD or DFT calculations in subsection II B.

These calculations are followed by a section devoted to stacks of 2D layers, with particular emphasis on graphene/graphene, hBN/hBN and graphene/hBN flexible bilayers. The individual layers are characterized by the graphene and hBN models developed in prior work [27–29, 32, 33] extended to incorporate out-of-plane deformations. A relatively simple coupling between the planes is introduced to match the stacking energies and distances between layers to those calculated in prior DFT calculations by Zhou *et al.* [1] as a continuous function of the stacking orientation. The end result of this work is the development of continuum models for large scale systems incorporating elasticity and plasticity. The models are parametrized for graphene, hBN and their bilayers.

The paper is organized as follows. Section II first introduces a 2D PFC model that allows for out of plane deformations and subsection II A shows that in the limit of small deformations it reduces to standard models of deformations in 2D sheets. Following this are applications to strained sheets, dislocation dipoles and grain boundaries. In Sec. III modeling of the coupling of multiple 2D layers is discussed in general and then applications to graphene/graphene hBN/hBN and graphene/hBN bilayers are presented. Parameters introduced in these models are fit to DFT calculations of Zhou *et al.* [1]. Sample applications to twisted bilayers and the influence of a defected layer on another layer are also presented for graphene/graphene system in this section. This is followed by a discussion of the results and conclusions in Sec. IV.

II. MODEL OF A FLEXIBLE 2D SHEET WITH CRYSTAL STRUCTURE.

The free energy functional in the original PFC [24–26] (or conserved Swift-Hohenberg [41]) model, $\mathcal{F}_n$, can be written as,

$$\frac{\mathcal{F}_n}{c_g} = \int d\vec{r}\left[\frac{\Delta B}{2}n^2 + \frac{B^x}{2}(\mathcal{L}n)^2 + \frac{\tau}{3}n^3 + \frac{v}{4}n^4\right] \quad (1)$$

where $\mathcal{L}$ is the operator $1 + \nabla^2_{xyz}$. ∇^2_{xyz} is the traditional Lapacian in Cartesian coordinates and c_g sets the energy scale. For certain parameters this free energy is minimized by a hexagonal (triangular) lattice for $\tau > 0$ ($\tau < 0$) in 2D and a BCC lattice in three dimensions. More complex forms of the operator $\mathcal{L}$ have been proposed for other crystal symmetries such as all five 2D Bravais lattices [42], chiral lattices [43], quasicrystals [44, 45] in 2D and FCC, and simple cubic and diamond lattices [46–49] in 3D. For the purposes of this work the simple free energy given in Eq. (1) will be used as the starting point.

Consider a flexible 2D sheet parameterized by the Cartesian coordinates (x, y) with height $h(x, y)$ denoting deviations from the (x, y) plane, which is assumed to be single valued, i.e., a Monge gauge is employed. Transforming from the Cartesian coordinates $\vec{r} = (x, y, z)$ to the sheet coordinates

$\vec{w} = (x, y, h(x, y))$ leads to integration in the sheet's plane of the form $\int d\vec{r} \to \int d\vec{r}\, J$, where J is the Jacobian determinant of the transformation and now $d\vec{r} \equiv dx\, dy$. This implies that the total density difference of the system is

$$n_{\rm tot} = \int d\vec{r}\, Jn, \tag{2}$$

and as such it is convenient to introduce an in plane density n_h such that

$$n_h \equiv Jn, \tag{3}$$

with corresponding conservation law $\partial_t \int d\vec{r}\, n_h = 0$. The free energy functional then becomes,

$$\frac{\mathcal{F}_h}{c_g} = \int d\vec{r} J \left[\frac{\Delta B}{2} \frac{n_h^2}{J^2} + \frac{B^x}{2} \left(\mathcal{L}_w \frac{n_h}{J} \right)^2 + \frac{\tau}{3} \frac{n_h^3}{J^3} + \frac{v}{4} \frac{n_h^4}{J^4} + \frac{\kappa}{2} (\nabla^2 h)^2 \right] \tag{4}$$

where $\mathcal{L}_w \equiv 1 + \nabla_w^2$ and ∇_w^2 is the Laplacian in the $\vec{w}$ coordinates as described in App. (A). The last term has been added to include bending energy and the parameter κ is the bending energy coefficient. It is assumed that the dynamics are dissipative and driven to minimize the total free energy functional such that the dynamics for n_h are conservative, i.e.,

$$\frac{\partial n_h}{\partial t} = M_{n_h} \nabla^2 \mu_{n_h} \tag{5}$$

and non-conserved for h of the form,

$$\frac{\partial h}{\partial t} = -M_h \mu_h, \tag{6}$$

where M_{n_h} and M_h are phenomenological constants and

$$\mu_{n_h} \equiv \frac{\delta \mathcal{F}_h}{\delta n_h} \tag{7}$$

and

$$\mu_h \equiv \frac{\delta \mathcal{F}_h}{\delta h}. \tag{8}$$

To simplify calculations it will be assumed that gradients in h are small and the Laplacian operator can be approximated as (see Eqns. (A5) and (A6))

$$\nabla_w^2 \approx \nabla_{xy}^2 - (h_x^2 \partial_x^2 + h_y^2 \partial_y^2 + 2 h_x h_y \partial_x \partial_y), \tag{9}$$

where $h_x \equiv \partial h/\partial x$ and $h_y \equiv \partial h/\partial y$. To further simplify the model, it will be assumed that h varies on length scales much longer than the atomic spacing such that $\nabla_w^2 n_h/J \approx (\nabla_w^2 n_h)/J$. Finally all J-factors will be expanded to lowest order to obtain the final simplified free energy functional,

$$\frac{\mathcal{F}_h}{c_g} \approx \int d\vec{r} \left[\frac{\Delta B}{2} n_h^2 + \frac{B^x}{2} (\mathcal{L}_w n_h)^2 + \frac{\tau}{3} n_h^3 + \frac{v}{4} n_h^4 + \frac{\kappa}{2} (\nabla^2 h)^2 \right]. \tag{10}$$

One difficulty concerning Eq. (10) is the assumption that h varies on much larger lengths than n_h. Considering that the free energy contains a term $\propto (\nabla^2 h)^2$ it might be assumed that this would be enough to suppress fluctuations of h on atomic scales. Test simulations reveal the possibility of numerical instabilities at small length scales, however. To ensure that such fluctuations are explicitly suppressed the bending energy term will be replaced by the contribution,

$$\mathcal{F}_b = \frac{\kappa}{2} \int \int d\vec{r} d\vec{r}' C(|\vec{r} - \vec{r}'|) h(\vec{r}) h(\vec{r}') \tag{11}$$

where, C can be written in Fourier space as

$$C(k) = \begin{cases} k^4, & k < k_{\rm max}; \\ C_{\rm max}, & k > k_{\rm max}, \end{cases} \tag{12}$$

where $k_{\rm max}$ and $C_{\rm max}$ can be tuned to eliminate small scale fluctuations. Equation (1) typically selects patterns with wave vector $k \approx 1$, so $k_{\rm max} < 1$. To summarize, the final proposed free energy density is

$$\frac{\mathcal{F}}{c_g} = \int d\vec{r} \left[\frac{\Delta B}{2} n_h^2 + \frac{B^x}{2} (\mathcal{L}_w n_h)^2 + \frac{\tau}{3} n_h^3 + \frac{v}{4} n_h^4 + \frac{\kappa}{2} \int d\vec{r}' C(|\vec{r} - \vec{r}'|) h(\vec{r}) h(\vec{r}') \right] \tag{13}$$

Equations (5), (6) and (13) complete the model. Expressions for the functional derivatives that enter the equations of motion are given in App. (B).

A. Amplitude expansion and small deformation limits

In 2D the amplitude expansion as exposed by Goldenfeld *et al.* and others [50–54] is obtained by writing the density, n_h, in terms of complex amplitude, η_{kl}, i.e.,

$$n_h = n_0 + \sum_{kl} \eta_{kl} e^{i\vec{G}_{kl} \cdot \vec{r}} + \text{C.C.} \tag{14}$$

where C.C. stands for complex conjugate, $\vec{G}_{kl} = k\vec{q}_1 + l\vec{q}_2$, (k,l) are the Miller indices and $(\vec{q}_1, \vec{q}_2)$ are the principle reciprocal lattice vectors and n_0 is the average of n_h. It is assumed that the amplitudes vary on length scales much larger than the atomic spacing $\sim 2\pi/|\vec{G}_{01}|$. For a honeycomb (or triangular) lattice the principle reciprocal lattice vectors are $\vec{q}_1 = q_0(-\sqrt{3}/2, -1/2)$ and $\vec{q}_2 = q_0(0,1)$, where q_0 is the equilibrium wave vector and a lattice constant $a_x = 4\pi/(\sqrt{3}q_0)$. The minimal set of modes needed to construct the lattice are $\vec{G}_{10}, \vec{G}_{01}$ and $\vec{G}_{\bar{1}\bar{1}}$, where $\bar{k} \equiv -k$, etc.. For the free energy functional given in Eq. (13) in this lowest order mode expansion, $q_0 = 1$. As discussed previously the variable h is also assumed to be varying on such length scales. While the amplitudes generated from the polynomial terms in the free energy have been published in many papers [50–54] (and for other symmetries [55]), the term $(\mathcal{L}_w n)^2$ has not been considered.

Assuming h and η_{kl} are slow variables it is straightforward to show that this transforms as

$$\int d\vec{r}|(\mathcal{L}_w n)^2 \to 2\sum_{kl}\int d\vec{r}\,\Big|\Big((1-h_x^2)\mathcal{L}_{xx} + (1-h_y^2)\mathcal{L}_{yy} - 2h_xh_y\mathcal{L}_{xy} - (h_xG^x_{kl})^2 - (h_yG^y_{kl})^2 - h_xh_yG^x_{kl}G^y_{kl}\Big)\,\eta_{kl}\Big|^2 \qquad (15)$$

where $\mathcal{L}_{ab} \equiv \partial_a\partial_b + iG^a_{kl}\partial_a + iG^b_{kl}\partial_b$.

In the small deformation limit the complex amplitudes can be written,

$$\eta_{kl} = \phi e^{-i\vec{G}_{kl}\cdot\vec{u}} \qquad (16)$$

where $\vec{u}$ is the displacement vector that enters continuum elasticity theory. To lowest order ϕ is approximately constant and can be determined by minimizing the free energy functional in the limit $\vec{u} = 0$ with respect to ϕ and gives

$$\phi = \frac{3n_0v + \tau + \sqrt{\tau^2 - 15\Delta Bv - 4n_0v(6\tau + 9n_0v)}}{15v}. \qquad (17)$$

In the limit of small deformations (i.e., small gradients in the displacement and height fields), the elastic portion of the free energy is,

$$\frac{F_{\rm elas}}{c_g} = \int d\vec{r}\left[\left(\frac{9}{2}\left(U_{xx}^2 + U_{yy}^2\right) + 3U_{xx}U_{yy} + 6U_{xy}^2\right)B^x\phi^2 + \frac{\kappa}{2}|\nabla^2 h|^2\right). \qquad (18)$$

where the strain tensors, U_{ij} are given as,

$$U_{ij} = \frac{1}{2}\left(\partial_j u_i + \partial_i u_j + h_i h_j\right) \qquad (19)$$

Equation (18) along with the strains defined by Eq. (19) are consistent with free energy functionals used to study graphene sheets [38] and other flexible sheets [40]. Thus it is apparent that in the small deformation limit the model reduces to a well-known result. While this particular calculation was done for hexagonal (or triangular) symmetry, which is elastically isotropic, it could be repeated for other symmetries (square, rectangular, etc.) and the resulting free energy would respect that symmetry.

B. Applications

In the following sections several applications will be considered to validate the model and illustrate how it can be used to consider complex physical microstructure such as dislocation dipoles and grain boundaries. In all cases the in plane parameters used in Hirvonen *et al.* [27] for graphene (referred to as PFC1 in that work) will be used. The parameter set is $(c_{\rm g}, \Delta B, B^x, \tau, v, n_0) = (6.58{\rm eV}, -0.15, 1, 0.5/\sqrt{0.98/3}, 1, 0)$ and gives rise to equilibrium periodic structures with maxima in n forming a hexagonal lattice as depicted in Fig. 1. These parameters give very good agreement with 2D molecular dynamics (MD) calculations using an AIREBO potential for low angle grain boundary and polycrystal energies, but somewhat larger difference for high angle grain boundary energies. In addition this parameter set and model was shown [27] to reproduce the same 5/7 defect structures observed commonly in experiments and other simulations.

1. *Strained Sheet*

One simple analytic calculation that can be examined is that of a compressed sheet. Consider a sheet with an initial strain, ϵ, in the y direction in a periodic system. In this instance the sheet should buckle to reduce the compression. For large values of κ, h will be roughly sinusoidal, i.e., for a system of size L_y

$$h(y) = H\cos(Qy), \qquad (20)$$

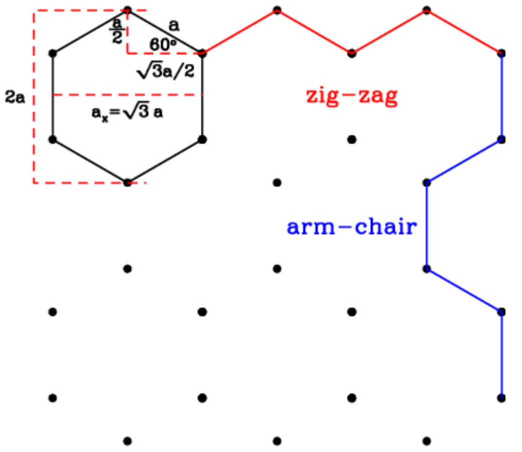

FIG. 1. Hexagonal geometry. For graphene $a_x \approx 2.56$ Å, while in dimensionless units the PFC model gives $a_x \approx 4\pi/\sqrt{3}$. The red (blue) lines illustrate zig-zag (arm-chair) directions.

where $Q = 2\pi/L_y$. Minimizing F_{elas} (i.e., Eq. 18) with respect to U_{yy}, subject to the boundary conditions $u_y(y = 0)$ and $u_y(y = L) = \epsilon L$ gives,

$$u_y(y) = \epsilon y + H^2 Q \sin(2Qy)/8 \qquad (21)$$

Equation (21) can be substituted into Eq. (18) to obtain the free energy per unit length,

$$\frac{F_{\rm elas}}{Lc_g} = \alpha\epsilon^2 + \frac{1}{2}\left(\frac{1}{2}\kappa Q^2 + \alpha\epsilon\right)(QH)^2 + \frac{\alpha}{16}(QH)^4 \qquad (22)$$

where $\alpha = 9B^x\phi^2/2$. Minimizing with respect to H gives

$$H^2 = -2\left(\frac{2\epsilon}{Q^2} + \frac{\kappa}{\alpha}\right). \qquad (23)$$

Substitution of Eq. (23) into Eq. (22) gives

$$\frac{F_{\rm elas}}{Lc_g} = -\kappa Q^2\left(\epsilon + \frac{\kappa Q^2}{4\alpha}\right). \qquad (24)$$

This gives a critical value of κ, $\kappa_{\rm c}$, for which no out of plane deformation will take place of,

$$\kappa_{\rm c} = -\frac{2\alpha}{Q^2}\epsilon. \qquad (25)$$

The above results imply that a solution only exists for a compressive stress, i.e., if $\varepsilon < 0$, as expected.

To test these predictions with the full model, simulations were conducted in a periodic domain using semi-implicit spectral methods [56] with a mesh size $\Delta x \approx \Delta y \approx 0.48$. The exact values were chosen to perfectly fit the periodic lattice in the simulation box. Simulations were constructed for a compressed sheet with an initial strain of $\epsilon = (a_0 - a_{\rm eq})/a_{\rm eq} = -0.0219$. The height of the layer, H, as defined by Eq. (20) was measured as a function of κ and compared with Eq. (23). This comparison is shown in Fig. 2. As can be seen in this figure the numerical results are quite close to the theoretical prediction, but there are some deviations. These deviations are likely be due to using a lowest order mode approximation in Eq. (14). It is interesting to note that if the magnitude ϕ is taken as an adjustable parameter the fits become very good as shown in Fig. 2.

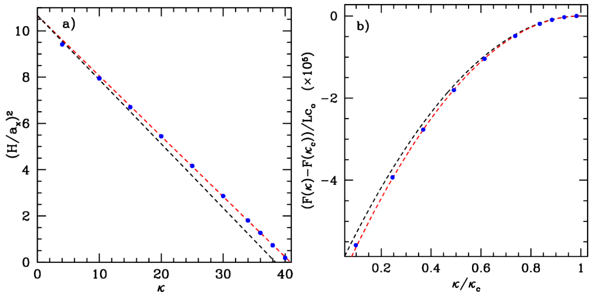

FIG. 2. In a) and b) the maximum height H and free energy difference of the buckled sheet are shown as function of the bending energy coefficient κ, respectively. The blue points correspond to the numerical simulations. The dashed black line corresponds to predictions from Eqs. (23) and (24) using the approximate analytic form for ϕ given by Eq. (17). The dashed red line corresponds to Eq. (23) using a ϕ that is 1.031 times that given in Eq. (17).

2. *Dislocation Dipole in Graphene*

Dislocations play a key role in determining material properties and grain boundary structures [18, 20, 32]. In graphene the dislocations often form a Stone-Wales defect which is comprised of a a 5/7 pair of rings instead of the 6 ring equilibrium honeycomb structure that is illustrated in Fig. 1. These defects create long-range elastic fields that can be significantly reduced in 2D materials by out of plane deformations. To examine this phenomena it is useful to first consider the case of a flat sheet (i.e., constant h). A honeycomb lattice is elastically isotropic and the displacement ($\vec{u}$) and stress ($\vec{\vec{\sigma}}$) fields due to an edge dislocation can be determined using classical elasticity theory (see for example Chaikin and Lubensky [57] chapter 9 section 3). The result is

$$\begin{aligned} u_x &= b\left(\theta + \sin(2\theta)/3\right)/2\pi; \\ u_y &= -b\left(\ln(r)/3 + \cos(2\theta)/3\right)/2\pi; \\ \sigma_{xx} &= -D\sin(\theta)(2+\cos(2\theta))/r; \\ \sigma_{yy} &= D\sin(\theta)\cos(2\theta)/r; \\ \sigma_{xy} &= D\cos(\theta)\cos(2\theta)/r, \end{aligned} \tag{26}$$

where for Eq. (18) $D = 2bc_{\rm g}B^x\phi^2/\pi$ and b is the magnitude of the Burgers vector which is $b = a_x$ for an edge dislocation. Integrating the free energy over $\theta = 0, 2\pi$ and $r = a_x, L$ gives the elastic energy of a dislocation, $F^{\rm elas}_{\rm disl}$,

$$\frac{F^{\rm elas}_{\rm disl}}{c_{\rm g}} = \frac{b^2 B^x \phi^2}{\pi}\ln\frac{L}{a_x}. \tag{27}$$

For a dislocation pair the elastic energy would be approximately twice this value when far enough apart.

To examine the influence of out-of-plane deformations, simulations of a dislocation dipole were undertaken using the same parameters as the previous section. For these simulations a system of size (L_x, L_y) was considered such that $L_x = (N+1/2)a_x$, $L_y = Ma_y$, $L_x/\Delta x = L_y/\Delta y$ with N and M integers, a_x and a_y the equilibrium lattice constants in the x and y directions (i.e., $a_y = \sqrt{3}a_x$) respectively. To create the pair, in the middle (top/bottom) half of the simulation $a^{\rm m}_x = L_x/N$ ($a^{\rm t}_x = L_x/(N+1)$) implying N ($N+1$) rows of atoms in the middle (top/bottom). This configuration includes a net bulk strain that goes to zero as $N \to \infty$. Mesh sizes $(\Delta x, \Delta y) \approx (0.48, 0.48)$ were chosen to be exactly compatible with the period boundary conditions in both directions. The bulk strain is

$$\varepsilon_{\rm m,t} = \frac{a^{\rm m,t}_x - a_x}{a_x} = \pm\frac{1}{2N}, \tag{28}$$

where the + (−) sign corresponds to the middle (top/bottom) layer. To measure the energy of the defect pair the energy of the bulk strained state was first determined by averaging the corresponding free energy density, $f_{\rm m}$ ($f_{\rm t}$) for N ($N+1$) rows. This bulk energy scales as $\approx 1/(2N)^2$ since the strain energy scales as the square of the strain. This is illustrated in Fig. 3. The free energy of the dislocation dipole, $F_{\rm d}$ was then taken as the total free energy minus the energy of the strained state, i.e.,

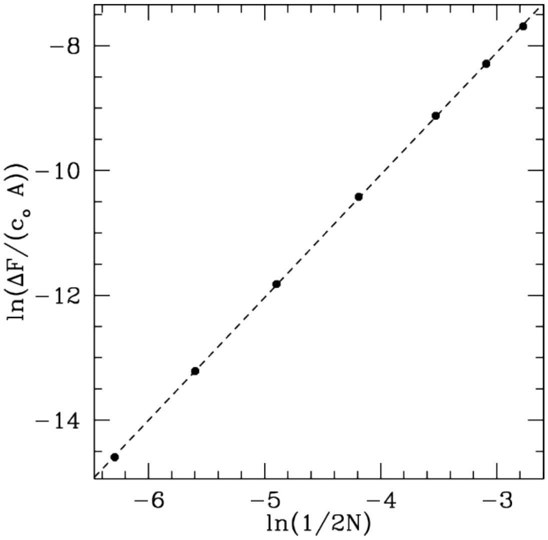

FIG. 3. Free energy density difference between strained and unstrained states as a function of system size. The slope of the best fit line (dashed line) is 1.96.

$$F_{\rm d} = F_{\rm tot} - \frac{L_x L_y}{2}(f_{\rm m} + f_{\rm t}). \tag{29}$$

Numerical simulations were conducted for the flat case ($\kappa \to \infty$), for $\kappa = \kappa_{\rm G}$, and $\kappa = 4\kappa_{\rm G}$, where $\kappa_{\rm G}$ was chosen to match that used in a recent study of graphene bilayers by Dai *et al.* [58], $c_{\rm g}\kappa_{\rm G} = 1.38$ eV which was used by Chen and Chrzan [59] in their continuum simulations of dislocations in graphene. Systems sizes ranged from smallest containing only 43 unit cells up to the largest of approximately 45,000 unit cells. The fields n and h were evolved via Eqs. (5) and (6) until the free energy per unit area was constant. In principle the dynamics should lead to the annihilation of the defect pair if the system size is too small, however the symmetry of the initial condition avoids this result.

To compare Eq. (26) with numerically simulated results for $h = 0$ it is useful to note that for the continuum result, $\sigma_{xx}(0, y) = \sigma_{yy}(0, y) = -\sigma_{xy}(x, 0) = -D/r$ for $(x, y) > 0$ and D/r for $(x, y) < 0$. To make a comparison of the numerical results from the PFC

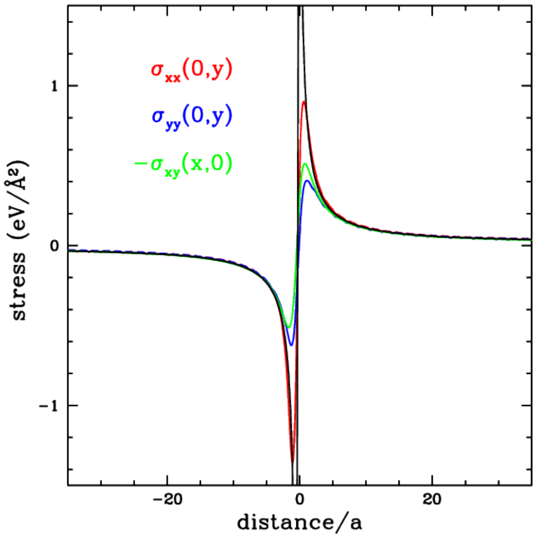

FIG. 4. Comparison of simulated stress fields (red, blue and green) with continuum (black) results, i.e., Eq. (26) close to the dislocation core for a flat sheet.

model with the analytic calculations, the stress fields must be calculated from the numerically obtained density deviations, n. The method to achieve this follows that of Refs. [60–62] as discussed in App. C. It should be noted that the continuum mechanics result diverges at the dislocation core, while the PFC result naturally regularizes the core leading to only finite stresses as discussed in prior work [62, 63]. The comparison is given in Fig. 4 which shows very good agreement for distances several atomic spacing away from the dislocation core for a system containing approximately $45,000$ unit cells.

When κ is finite the height, h, of the film can vary to reduce the stress in compressed regions. Portions of a sample simulation are shown in Fig. 5 for the fields n_h, h, h_x and h_y centered around one of the two 5/7 dislocation cores. As can be seen in this figure h_x and h_y are close to zero above the core and vary considerably below or near the dislocation core. This is due to the fact that the strain is tensile above and compressive below.

For a more detailed comparison Fig. 6 shows the stress fields for a portion of a system of total size $(70a_x \times 40a_y)$ for $\kappa = \infty$ (i.e., $h = 0$), the continuum result Eqs. 26 and for $\kappa = \kappa_{\rm G}$. Similar to Fig. 4 there is close agreement between the continuum and simulated results for $h = 0$ except close

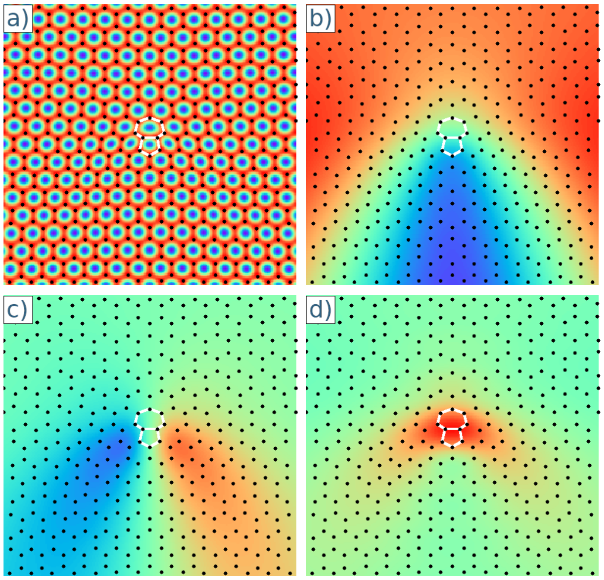

FIG. 5. Portion $(13.3a_x \times 13.3a_x)$ of sample the field h and it's gradients around one of the dislocations for a system contained $2,800$ unit cells. In a), b), c) and d) n_h, h h_x and h_y are shown for $\kappa = \kappa_{\rm G}$. In each figure black dots are placed at maxima of n and bonds for the 5/7 Stone-Wales defect are drawn in white. In c) and d) the colour scale is such that red, green and blue correspond to $h_x = 0.5, 0$ and -0.5 respectively and similarly for h_y.

to the dislocation core. The figure also indicates a large reduction in the stress fields for $\kappa = \kappa_{\rm G}$ as expected. A further comparison of $\sigma_{xx}(0,y)$, $\sigma_{yy}(0,y)$ and $\sigma_{xy}(x,0)$ is shown in Fig. 7 for this system size. This figure demonstrates a dramatic reduction in compressive stress (.i.e., $\sigma_{ii} < 0$) and relatively little for tensile stress (i.e., $\sigma_{ii} > 0$) as out of plane deformations cannot reduce tensile stress.

Finally, the total free energy of the of the dislocation pairs was measured as function of system size for $\kappa = \infty, 4\kappa_{\rm G}$ and $\kappa_{\rm G}$ as shown in Fig. 8. The results for the flat sheet ($\kappa = \infty$) are in close agreement with the continuum prediction, i.e., twice Eq. 27. The figure also shows a large reduction in energy as κ is decreased from ∞ to $4\kappa_{\rm G}$ to $\kappa_{\rm G}$. It is interesting to note that the results for $\kappa = \infty$ imply that the energy of a dislocation pair becomes infinite as $L \to \infty$. In contrast the pair free energy seems start to level off or saturate for large system sizes if buckling is allowed. Empirically such an $F_{\rm pair}$ for $\kappa = \kappa_{\rm G}$ fits the line $F_{\rm pair} = [13.6 - 19.0(a_x/L)^{1/3}]$

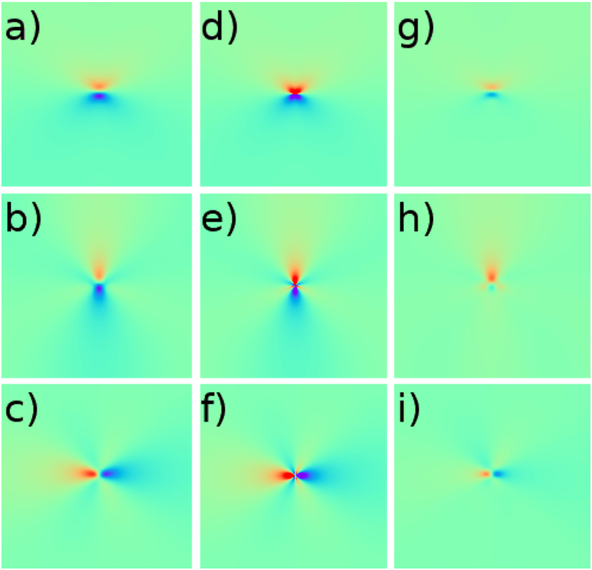

FIG. 6. Portion ($35a_x \times 35a_x$) of sample stress fields around one of the dislocations for a system of size (size ($1024\Delta x \times 1024\Delta y$). In a), b) and c) σ_{xx}, σ_{yy} and σ_{xy} are shown for a flat ($h = 0$) layer. In d), e) and f) the strain fields are shown for the continuum predictions, Eq. (26) and in g), h) and i) the fields are shown for $\kappa = \kappa_G$.

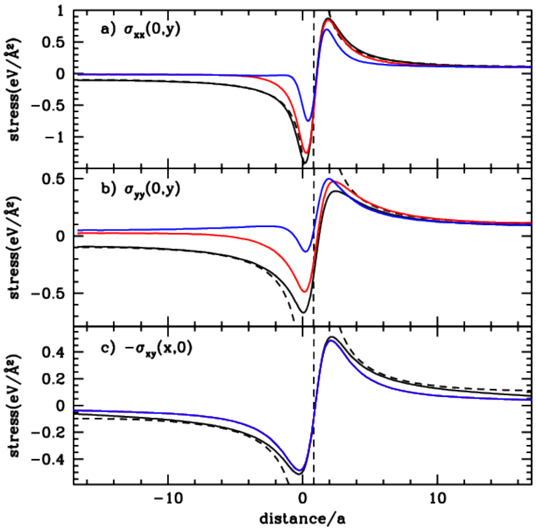

FIG. 7. Comparison of simulated stress fields with continuum mechanics prediction (dashed black line) and $\kappa = \infty$ (black line), $4\kappa_G$ (red line) and κ_G (blue line).

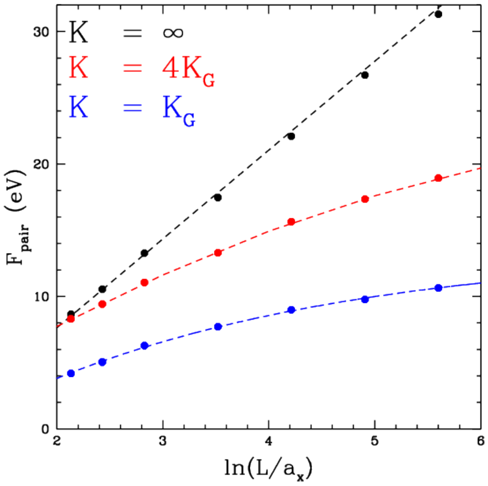

FIG. 8. Free energy of dislocation dipole as a function of system size. In this figure the points are the numerical results and the black dashed line is the continuum elasticity result, twice that in Eq. (27). The red and blue dashed lines are guides to the eye.

eV which gives a pair energy in the limit of infinite system size of 13.6 eV. This implies that the energy of a 5/7 dislocation in graphene is approximately 6.8 eV. The change from logarithmic ($\kappa = \infty$) to saturation (finite κ) as a function of system size is consistent with the continuum calculations of Seung and Nelson [39] and Chen and Chrzan [59]. In the latter article molecular dynamics simulations were also conducted using a REBO potential [64] which also gave similar behavior. The magnitude of the 5/7 defect dislocation energy is similar to values obtained by Chen and Chrzan [59] (6.17 eV), Yazyev and Louie [30] using *ab initio* calculations (7.5 eV) and from molecular dynamics simulations using a AIREBO potential [65] from Liu and Yakobson [66] (5.0 eV).

3. *Grain Boundary Energy*

In this section the role of out of plane deformation on symmetric tilt grain boundary energies is examined in a simulation box of size $L_x \times L_y$. A grain is set up by rotating the top half of the simulation box by an angle θ and the bottom half by $-\theta$ to create a symmetric tilt boundary with net difference rotation angle of 2θ. The system size is chosen to fit perfectly in the x direction. Periodic boundary conditions are used in the x and y directions. To have perfect periodicity in the x-direction for the zig-zag orientation system size must satisfy the condition

$$L_x^{zz} = a_x\sqrt{3(l+1/2)^2 + (k+1/2)^2}, \tag{30}$$

for a rotation angle of

$$\theta^{zz} = \arctan\left(\frac{\sqrt{3}(l+1/2)}{k+1/2}\right), \tag{31}$$

where k and l are integers as illustrate in Fig. 9(a). Another choice is given for the n, m pairs as also shown in this 9(b). For the armchair orientation the system size in the x-direction is given by

$$L_x^{ac} = a_x\sqrt{3(k+1/2)^2 + (l+1/2)^2}, \tag{32}$$

for a rotation angle of

$$\theta^{ac} = \arctan\left(\frac{(l+1/2)}{\sqrt{3}(k+1/2)}\right), \tag{33}$$

where k and l are integers as illustrated in Fig. 9(a).

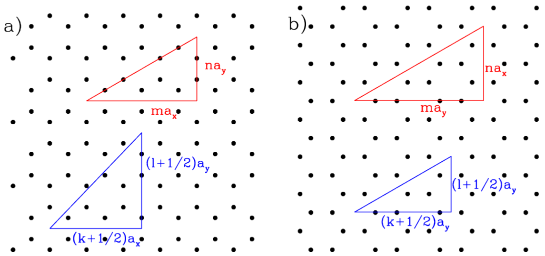

FIG. 9. Illustration of possible rotations for zig-zag (a) and armchair (b) orientations.

The grain boundary energy per unit length, γ, is defined to be

$$\gamma = (F_{\rm GB} - F_{\rm eq})/(2L) \tag{34}$$

where $F_{\rm GB}$, $F_{\rm eq}$ and L are the energy of the system containing a grain boundary, the energy of a perfect crystal and the length of the boundary, respectively. It should be noted that the periodic box contains two grain boundaries which explains the factor of 2 in the denominator. The grain boundary energy as function of angle is shown in Fig. 10. As can be seen from this figure out of plane deformations allow the system to somewhat lower the grain boundary energies but less than what has been observed in low temperature MD simulations [27].

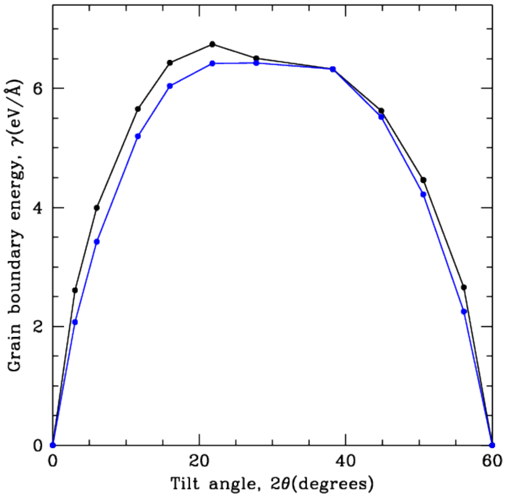

FIG. 10. Grain boundary energy for $\kappa = \infty$ (black) and $\kappa = \kappa_{\rm G}$ (blue).

III. MULTIPLE LAYERS

The purpose of this section is to illustrate how multiple layers can be modeled and parameterized to match the stacking energies and heights as a function of stacking position. In absence of experimental data it is not obvious what the energies and heights should be matched to, since DFT data depend on the specific type of DFT model and are done at zero temperature, while the MD data depend on level of approximation of the potentials developed. As illustrated by Zhou *et al.* [1] different DFT calculations can differ by 10% or more in stacking heights and up to 30% in stacking energy densities. With this in mind the fitting will be done using a one-mode approximation for the density field which allows for analytical results. This fitting will highlight how the PFC model presented in this section can be fitted quite close to a given DFT calculation. If an more accurate fit were deemed important it would be useful to go beyond a one-mode approximation, which may require numerical work.

To model multiple layers it is assumed that each individual layer has a free energy of the form given in Eq. (13) such that the parameters that enter are determined by the make-up of the i^{th} layer. In addition to this, a coupling between nearest layers is added for N layers with densities n_i and heights h_i

of the form,

$$\mathcal{F}_{\rm c} = F_{\rm st} + F_{\Delta h} \tag{35}$$

where $F_{\rm st}$ and $F_{\Delta h}$ correspond to energies associated with stacking and height between layers, which in the simplest cases can be approximated as,

$$F_{\rm st} = \sum_{i=1,j>i} \int d\vec{r}\, V_{ij} \delta n_i \delta n_j, \tag{36}$$

and

$$F_{\Delta h} = \sum_{i=1,j>i} \int d\vec{r}\, a_2^{ij} (\Delta h_{ij} - \Delta h_{ij}^0)^2. \tag{37}$$

where $\delta n_i = n_i - \bar{n}_i$ and $\bar{n}_i$ is the average of n_i. Here V_{ij} determines the stacking energy of the layers, Δh_{ij}^0 is the reference distance between the i^{th} and j^{th} layers and a_2^{ij} controls the energy cost for deviations from the equilibrium layer spacings. Of course (as discussed in subsections III B and III C) the coupling is more complex when an individual layer is made up of more than one element. In principle a more complex form could be used, which would be particularly important if the layers were to be ripped apart (note in this parabolic approximation that energy is infinite). This particular form is only valid for small deviations from the equilibrium position.

The work of Zhou *et al.* [1] will be used to determine the parameters that enter $\mathcal{F}_{\rm c}$. In this work the researchers considered four specific methods that rely on density functional theory (DFT) and various corrections. These methods are given the names, DFT-D2, vdW-DF2, MGGA-MS2 and ACFDT-RPA whose details can be found in Ref. [1]. The conclusions of this detailed study was that the computationally expensive ACFDT-RPA method was deemed the best in reproducing various material properties. For this reason the parameters that enter $\mathcal{F}_{\rm c}$ will be chosen to best match the ACFDT-RPA results. To illustrate this approach graphene/graphene, hBN/hBN and graphene/hBN bilayers will be consider in the following subsections.

A. Monatomic/monatomic bilayer (graphene/graphene)

In this subsection the graphene/graphene bilayer system is considered. Graphene forms a hexagonal lattice as illustrated in Fig. 1 where nearest neighbour atoms are a distance a apart. In this system the coupling of the layer can be accounted for by a stacking free energy of the form,

$$F_{\rm st} = V_0 \int d\vec{r}\, \delta n_1 \delta n_2, \tag{38}$$

and a spacing free energy of

$$F_{\Delta h} = a_2 \int d\vec{r}\, (\Delta h - \Delta h^0)^2, \tag{39}$$

where

$$\Delta h^0 = \Delta(1 + \alpha \delta n_1 \delta n_2), \tag{40}$$

where h_1 (h_2) are heights of the layers, $\Delta h = h_2 - h_1$, and Δh^0 is the reference distance between the two layers. In order to parameterize this model, $V_{\rm g}$, a_2, Δ and α must be determined. As discussed above these parameters will be chosen to best match the prediction of the ACFDT-RPA calculations of Zhou *et al.* [1].

To make a connection with the PFC type model presented in this work, it is useful to consider a one mode expansion of the PFC model, which for graphene takes the form,

$$\begin{aligned} n_1 &= \bar{n}_1 - \phi \sum_{kl} \left[e^{i\vec{G}_{kl}\cdot\vec{r}} + \text{C.C.} \right]; \\ n_2 &= \bar{n}_2 - \phi \sum_{kl} \left[e^{i\vec{G}_{kl}\cdot(\vec{r}+\vec{r}_o+a\hat{y})} + \text{C.C.} \right], \end{aligned} \tag{41}$$

where $\vec{G}_{kl} = k\vec{q}_1 + l\vec{q}_2$, $\vec{q}_1 = -(\sqrt{3}\hat{x}, \hat{y})/2$, $\vec{q}_2 = \hat{y}$ and k and l are the Miller indices and take on integer values. For $\phi > 0$ Eq. (41) leads to a hexagonal lattice structure. For $\vec{r}_0 = 0$ the stacking is AB. Setting $\vec{r}_0 = (0, y_0)$ and increasing y_0 takes the system through various stackings as depicted in Fig. 11.

The energy of separation between the layers is given in Eq. (39), using Eq. (40) for Δh^0. Integrating over a unit cell and minimizing with respect to Δh gives a separation distance ($\Delta h^{\rm eq}$) of

$$\begin{aligned} \Delta h^{\rm eq} = \Delta\Big(1 - \alpha\frac{\phi^2}{\sqrt{3}}\big[&2\sqrt{3}\cos(y_0/2)(1+\cos(y_0/2)) \\ &+6\sin(y_0/2)(1-\cos(y_0/2)) - \sqrt{3}\big]\Big), \end{aligned} \tag{42}$$

and matching to Zhou *et al.* [1] gives $\Delta = 3.56$ Å and $\alpha = 0.26$. Δ can be converted to dimensionless units ($\Delta_{\rm d}$) by noting that in graphene $a_x = 2.56$

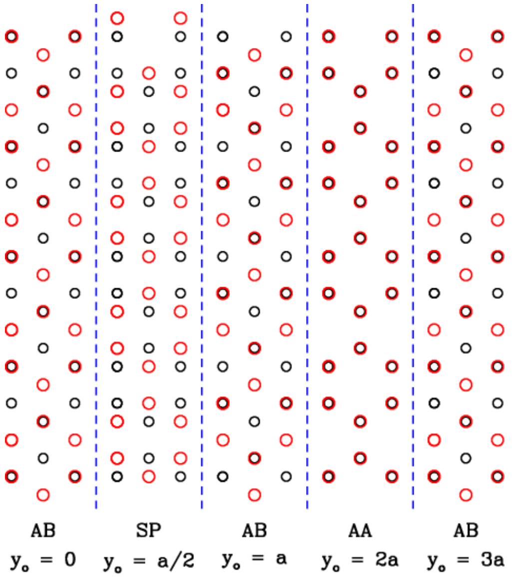

FIG. 11. Stacking for graphene/graphene bilayer using the notation of Zhuo *et al.* [1]

Å, while in the one mode PFC model $a_x = 4\pi/\sqrt{3}$. This gives $\Delta_{\rm d} = 10.08$. The contribution to the free energy at $h = h_{\rm eq}$ is,

$$F_{\Delta h}/A = 4a_2\Delta^2\phi^4\alpha^2\Big(8\cos(y_0/2)^3 - \cos(y_0/2)^2 -7\cos(y_0/2) + \sqrt{3}\sin(y_0/2)(\cos(y_0/2)-1) +9\Big). \tag{43}$$

A comparison of Eq. (42) (labeled PFC 1st order in the figures) with the calculations of Zhou *et al.* [1] is shown in Fig. 12. In doing the matching it was not possible to exactly fit to the ACFDT-RPA calculations as the PFC model tended to overestimate the AA and underestimate the SP spacing. Nevertheless, considering the deviations of the different DFT calculations, the fit is quite good. It is possible to get a better fit by introducing higher order terms in Δh^0 that enter $\mathcal{F}_{\Delta h}$. For example, if the following is used

$$\Delta h^0 = \Delta[1+\alpha\delta n_1\delta n_2+\beta(\delta n_1\delta n_2)^2], \tag{44}$$

then matching the Δh that minimizes the free energy to the height at AB ($h_{\rm AB} \approx 3.39$ Å), SP ($h_{\rm SP} \approx 3.43$ Å) and AA ($h_{\rm AB} \approx 3.62$) stackings gives,

$$\Delta = \frac{1}{18}\left(h_{\rm AA}+45h_{\rm SP}-28h_{\rm AB}\right) = 3.50; \mathring{A}$$
$$\alpha = \frac{19h_{\rm AA}+45h_{\rm SP}-64h_{\rm AB}}{12\phi^2(h_{\rm AA}+45h_{\rm SP}-28h_{\rm AB})} = 0.269;$$
$$\beta = \frac{h_{\rm AA}-h_{\rm SP}+8h_{\rm AB}}{12\phi^2(h_{\rm AA}+45h_{\rm SP}-28h_{\rm AB})} = -0.187,$$

using the PFC model parameters for graphene. This second-order fit is also shown in Fig. 12 and gives very good agreement with the ACFDT-RPA data. Also included in this figure is a result obtained from a numerical calculation in which the AB state is first relaxed using the PFC 1st order parameters and then shifted to other stackings and the height is left to relax. It should be noted that if the density is allowed to relax it will lead the system to fall into the lower energy AB state, except exactly at the SP or AA state in which long lived states can exist due to symmetry. As seen in Fig. 12 the numerical results are quite close the theoretical ones.

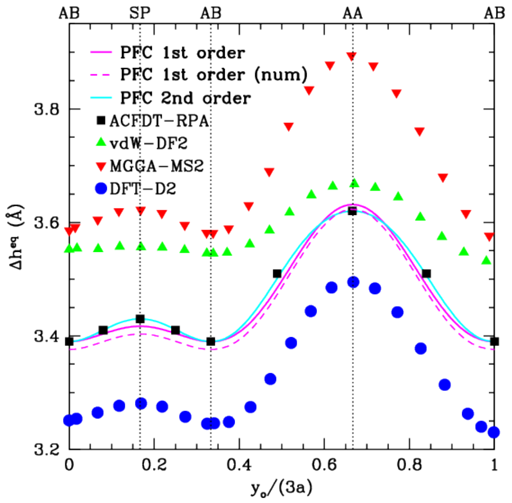

FIG. 12. Equilibrium height as a function of stacking location for graphene/graphene bilayer, for the PFC model and various DFT calculations of Zhou *et al.* [1]. The solid purple and dashed cyan lines correspond to PFC 1st (i.e., Eq. (42)) and 2nd (i.e., Eq. (44)) respectively.

To estimate the constant a_2, consider the effective coupling introduced by Zhou *et al.* [1], i.e.,

$$\Gamma = Ae^{-\alpha h} - B\left(\frac{d_\ell}{h}\right)^4 + \gamma_{\rm coh} \tag{45}$$

where

$$\alpha = -\frac{\zeta + \sqrt{\zeta^2 + 64\kappa_0 d_\ell^2 \Delta\gamma}}{8 d_\ell \Delta\gamma};$$
$$A = \frac{4\Delta\gamma e^{\alpha d_\ell}}{4 - \alpha d_\ell};$$
$$B = \frac{\alpha d_\ell \Delta\gamma}{4 - \alpha d_\ell}, \qquad (46)$$

$\zeta = [\kappa_0 d_\ell^2 - 20\Delta\gamma]$ and $\Delta\gamma = \gamma - \gamma_{\rm coh}$, and d_ℓ is the layer spacing. Expanding around $h = d_\ell$ for the AB configuration (i.e., $\gamma = \gamma_{\rm coh}$), gives,

$$\Gamma \approx a_2(h - d_\ell)^2 + a_3(h - d_\ell)^3 + a_4(h - d_\ell)^4 + \qquad (47)$$

where

$$a_2 = \frac{Ae^{-\alpha d_\ell}(\alpha d_\ell)^2 - 20B}{d_\ell^2 2!} = 0.442\frac{\rm mJ}{\rm m^2 Å^2} = 0.276\frac{\rm eV}{\rm nm^4};$$
$$a_3 = \frac{-Ae^{-\alpha d_\ell}(\alpha d_\ell)^3 + 120B}{d_\ell^3 3!} = -0.405\frac{\rm mJ}{\rm m^2 Å^3};$$
$$a_4 = \frac{Ae^{-\alpha d_\ell}(\alpha d_\ell)^4 - 840B}{d_\ell^4 4!} = 0.203\frac{\rm mJ}{\rm m^2 Å^4}. \qquad (48)$$

A comparison of the fits to the ACFDT-RPA data is shown in Fig. 13. In addition the coupling is shown for various stackings in Fig. 14, to order $(h - d_\ell)^2$. When constructing the potentials Zhou *et al.* uses the DFT-D2 calculations instead of the more accurate ACFDT-RPA for computational efficiency. Since there are no such difficulties with the PFC model, the ACFDT-RPA data was used to parameterize a_2. To convert to dimensionless units

$$a_{2d} = a_2 \frac{6.242 \times 10^{18}\rm eV}{\rm J} \frac{(\rm m)^2}{(10^{10}Å)^2} \frac{1}{6.58\rm eV} \frac{(2.56Å)^4}{(4\pi/\sqrt{3})^4}$$
$$= 6.51 \times 10^{-5} \qquad (49)$$

To obtain an approximate value for V_0 Eqs. (41) are substituted into Eq. (38) and then integrated over a unit cell and divided by the area of it. The result is

$$\frac{\Delta F_{\rm st}}{A} = 2V_0\phi^2\left(1 - \cos\left(\frac{y_0}{2}\right)\right)\left(2 + \cos\left(\frac{y_0}{2}\right)\right.$$
$$\left. -\sqrt{3}\sin\left(\frac{y_0}{2}\right)\right), \qquad (50)$$

where $\Delta F_{\rm st} = F_{\rm st}(y_0) - F_{\rm st}(y_0 = 0)$. The total energy is then $F_{\rm c} = F_{\rm st} + F_{\Delta h}$. A value of $V_0 = 1.29$ eV/nm^2 resulted in the best match to the ACFDT-RPA data of Zhou *et al.* [1] as shown in Fig. 15.

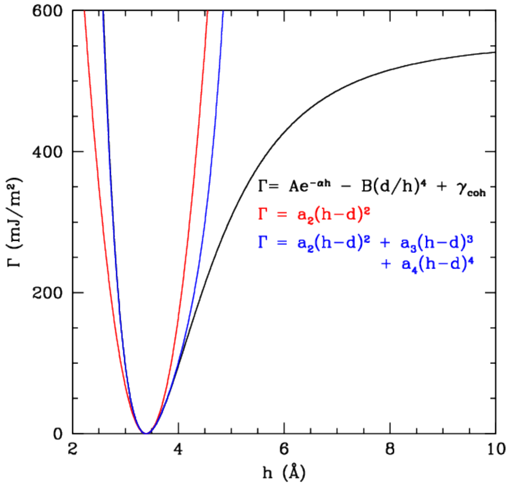

FIG. 13. Comparison of Zhou *et al.* [1] potential and a polynomial expansion. We note that this is a fit to the ACFDT-RPA data and not to the DFT-D2 data that Zhou *et al.* fit to in Fig. 8.

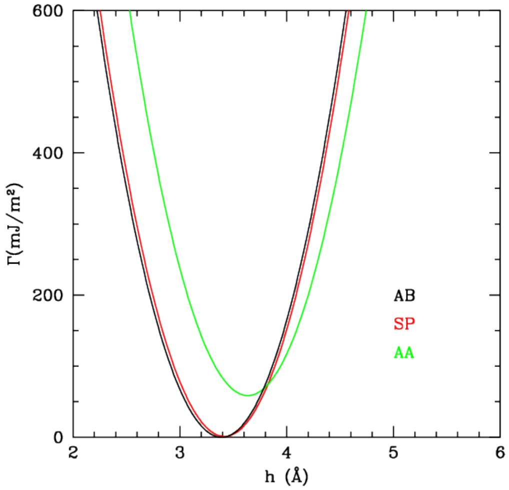

FIG. 14. Interaction for various stackings using a parabolic approximation.

As can be seen in this figure the fitting over (under) estimates the energy of the AA (SP) stacking but overall provides a reasonable approximation to the DFT calculations. In dimensionless units V_0 is $(V_{0\rm d})$,

$$V_{0\rm d} = \frac{V_0}{c_{\rm g}}\left(\frac{a_{\rm g}}{a_x}\right)^2 \qquad (51)$$

Quantity	Dimensional	Dimensionless
V_0	1.29 eV/nm^2	2.44×10^{-4}
a_2	0.276 eV/nm^4	6.51×10^{-5}
Δ	3.56 Å	10.08
α	–	0.26

TABLE I. Summary of model parameters for a graphene/graphene bilayer.

where $c_g = 6.58$ eV, $a_g = .256$ nm and $a_x = 4\pi/\sqrt{3}$, which gives

$$V_{0d} = 2.44\times10^{-4}. \tag{52}$$

A summary of the fitting parameters is given in Table I.

As with the height fitting it is possible to get a better fit by including higher order terms, for example if a stacking free energy of the form

$$\mathcal{F}_{st} = \int d\vec{r}[V_0^{(1)}\delta n_1\delta n_2 + V_0^{(2)}(\delta n_1\delta n_2)^2] \tag{53}$$

is used a better fit can be obtained. Matching to SP ($\Delta\mathcal{F}_{SP}/A \approx 9.42$ mJ/m^2) and AA ($\Delta\mathcal{F}_{AA}/A \approx 53.21$mJ/m^2) stacking energies densities gives,

$$V_0^{(1)} = \frac{19\Delta\mathcal{F}_{AA}/A + 45\Delta\mathcal{F}_{SP}}{216\phi^2} = 219.2 \text{ mJ/m}^2;$$
$$V_0^{(2)} = \frac{\Delta\mathcal{F}_{AA}/A - 9\Delta\mathcal{F}_{SP}}{216\phi^2} = -159.1 \text{ mJ/m}^2. \tag{54}$$

Fits to this second order form are shown in Fig. 15. As with the height calculations a numerically obtained solution using the PFC 1st order parameters is also included in this figure. The numerical result is worse that the analytic one and it is unlikely that adjusting the parameters would lead to a better fit to the ACDFT-RPA result. In this instance the PFC 2nd order model would provide more flexibility to numerical model a given DFT result.

A couple of points are worth mentioning. The fitting done here is different than that of Zhou *et al.* [1], in which the parameters that enter Γ in Eq. (45) depend on the stacking orientation and no other coupling is needed. In this work the stacking energy is fixed by F_{st} in a separate contribution to the free energy. As seen by the fitting of the stacking heights and energies this works quite well, partly due to the fact that $F_{st} << F_h$ which simplifies analytic calculations. Considering the large differences between the various DFT models an exact fitting to one of the models is unlikely going to lead to better quantitative predictions.

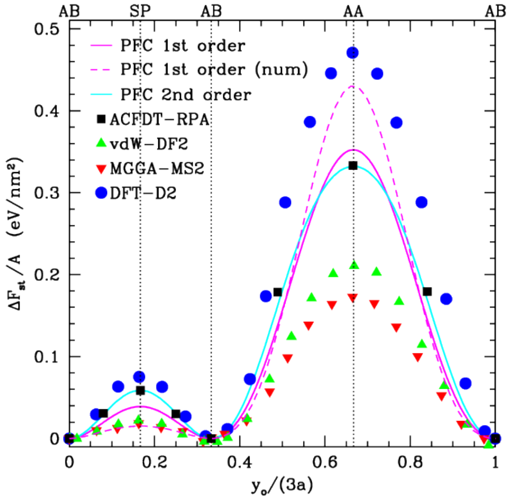

FIG. 15. Free energy difference as a function of stacking location for a graphene/graphene bilayer.

1. *Sample simulations*

Four types of simulations were conducted using the PFC 1st order model using the parameters derived in the one-mode approximation discussed in the previous section. The first case was to validate the model by reproducing known results and in latter three to illustrate how the model can be used to study complex structures. In the first case the layers of the bilayer were rotated with respect to each by an angle θ. This leads to a Moiré patterns as domain walls and junction form between commensurate regions. The junctions form a triangle pattern with a periodicity (λ) that is inversely proportional to θ such that $\lambda = a_x/(2\sin(\theta/2))$ in the absence of coupling between the layers [58, 67]. As seen in Fig. 16 such a pattern emerges in addition to the junctions moving out plane, such that, junctions on the top (bottom) layer bulge up (down). This is the so-called "breathing mode" observed and named by Zhou *et al.* [1], confirming the methodology presented in this work. Zhou *et al.* [1] also observed other modes, which may be explored in future work.

Simulations of phase boundaries in the zig-zag

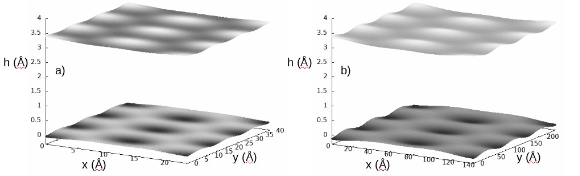

FIG. 16. In a) upper and lower layers have been rotated by an angle $+5.21^o$ and -5.21^o respectively and in b) the angles are $+1.87^o$ and -1.87^o.

(ZZ) and arm-chair (AC) directions (as depicted in Fig. 1) were conducted such that the bottom layer was a perfect crystal and the top layer had an AB stacking on the sides and a BA stacking in the middle. This leads to a domain wall at the boundary between the AB and BA stackings. As seen in experiments and simulations [68] the width of the domain wall (referred to as a soliton in reference [68] in the ZZ direction ($\sim$ 10 nm) was larger than in the AC direction ($\sim$ 6 nm). Small portions of the systems are depicted in Fig. 17. The widths (as determined by width of $h_2 - h_1$ at half of the maximum) are 9.2 nm and 7.7 nm for the ZZ and AC directions, respectively. These results are in qualitative agreement with Alden *et al.* [68] although the width of the AC domain wall is slightly larger. The larger width leads to a larger energy per unit length (defined as $(F_{\rm sol} - F_{\rm eq})/2L$, where $F_{\rm sol}$ is the energy of the system containing a domain wall in one layer, L is the length of the domain wall and the 2 is included as there are two domain walls in the simulation cell) for the ZZ domain wall, 0.17 eV/Å, as compared to 0.12 eV/Å for the AC case. As expected these boundaries are quite a bit smaller than that of a large angle grain boundary (see Fig. 10).

The model developed in this paper can handle more complex structures that contain dislocations and grain boundaries, not just small deformations about a perfect lattice. To examine the influence of defects in bilayers a perfect unrotated layer was placed on top of one containing a symmetric tilt grain boundary (using the same initial condition discussed in section II B 3). As the grain boundary forms in the bottom layer out of plane deformation occur to relieve elastic energy, which in turn causes the layer above to also deform in sync with the bottom layer. This is illustrated for a symmetric tilt grain boundary in Fig. 18 at a tilt angle of $\theta = 3.8^o$.

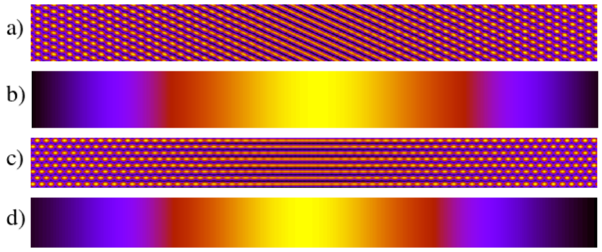

FIG. 17. Structure of a domain wall in zig-zag (a) and b)), and arm-chair (c) and d)) directions. In a) and c) the sum of the densities $(n_1 + n_2)$ is depicted while in b) and d) the difference of the height $(h_2 - h_1)$ is shown. In a) and b) the system size is 15 nm × 1.9 nm and in c) and d) 15 nm × 1.7 nm.

The grain boundary itself causes deformations on the scale of ± 2.0 Å which induces similar deformations in the upper layer, although to a slightly lesser extent. In addition the deformations in the upper layer slightly more smeared out. This is expected since deformations in a layer increases the elastic energy and hence the top layer will not buckle to same extent as the lower layer which contains the grain boundary. Since the top layer is not rotated and the bottom is, a Moiré pattern also emerges between the grain boundaries in both layers as expected, although it is barely discernible in the figures as deformations due to the grain boundary are much larger.

To further illustrate how the model presented in this work can examine very complex structures, a simulation was conducted to study the influence of a polycrystalline bottom layer on a perfect top layer. In this simulations the bottom layer initially contained sixteen grains separated by supercooled liquid. In these simulations $M_{n_h} = 1.0$ and $M_h = 25.0$. Sample configurations are shown in Fig. 19 at $t = 500$, 50 000 and 250 000 time steps. Since the top layer is not rotated Moiré patterns emerge in the layers in the breathing mode state previously discussed. As time evolves grain boundaries form between the grains and out-of-plane deformation start to increase to release stress at such boundaries. These deformations then cause the upper layer to deform in sync with the bottom layer as was the case of a simple grain boundary.

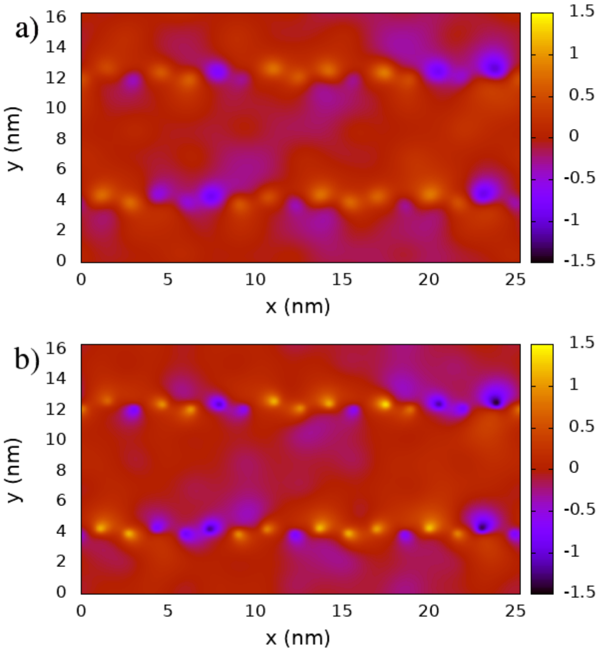

FIG. 18. Influence of grain boundary on overlayer. In b) the bottom layer is shown which contains a symmetric tilt grain boundary at angles 3.8^o, while a) shows the top layer. The color scale corresponds to the the deviations of the height from its mean of each layer in units of angstroms.

B. Binary/binary bilayers (hBN/hBN)

In the binary hBN/hBN system there are two different types of stackings and the first is shown in Fig. 20 in which an AA' stacking gives rise to a configuration where every A atom has a B atom as a nearest neighbour in the other layer. In Zhou *et al.* [1] this is referred to as a hBN/hBN1 stacking. The other stacking in shown in Fig. 21 and is referred to as the hBN/hBN2 stacking. In this instance the AA stacking leads to A (B) atoms sitting on top of A (B) atoms.

Using the binary model of Taha *et al.* [28, 29], as described in App. D it possible to repeat the calculations for a hBN bilayer. For this system Δh^0 can be written

$$\Delta h^0 = \Delta\Big[1 + \alpha_{\rm AA}\delta n_{\rm A1}\delta n_{\rm A2} + \alpha_{\rm BB}\delta n_{\rm B1}\delta n_{\rm B2} + \frac{\alpha_{\rm AB}}{2}\left(\delta n_{\rm A1}\delta n_{\rm B2} + \delta n_{\rm B1}\delta n_{\rm A2}\right)\Big], \quad (55)$$

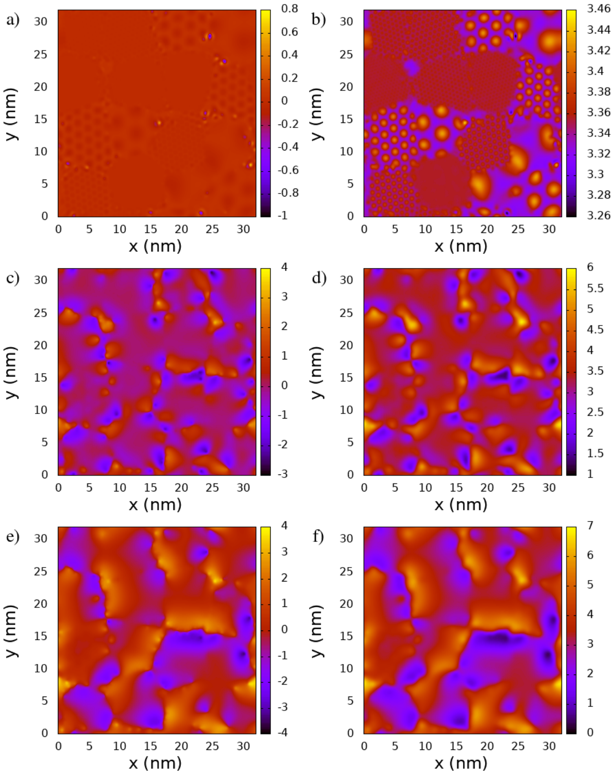

FIG. 19. Influence of grain structure at dimensionless time $t = 500$ in a) and b) for the bottom and top layer respectively. Similarly in c) and d) at time 50 000 and in e) and f) at 250 000 time steps. The color scale corresponds to the height of each layer in units of angstroms.

where A and B refer to the two binary components, 1 and 2 refer to the different layers and $\delta n_x \equiv n_x - \bar{n}_x$, where $\bar{n}_x$ is the average of n_x. Integrating $F_{\Delta h}$ over a unit cell and minimizing with respect to Δh gives for the hBN/hBN1 system,

$$\Delta h^{\rm eq} = \Delta\Big(1 - \frac{2\phi^2}{\sqrt{3}}\big[\Delta\alpha\sqrt{3}\cos(y_0/2)(1+\cos(y_0/2)) + 3\Delta\alpha_{\rm AB}\sin(y_0/2)(1-\cos(y_0/2)) + \Delta\alpha\phi^2\big]\Big) \quad (56)$$

where $\Delta\alpha \equiv \alpha_{\rm AA} + \alpha_{\rm BB} - 2\alpha_{\rm AB}$, and $\Delta\alpha_{\rm AB} \equiv \alpha_{\rm AA} - \alpha_{\rm BB}$. The free energy associated with this term in

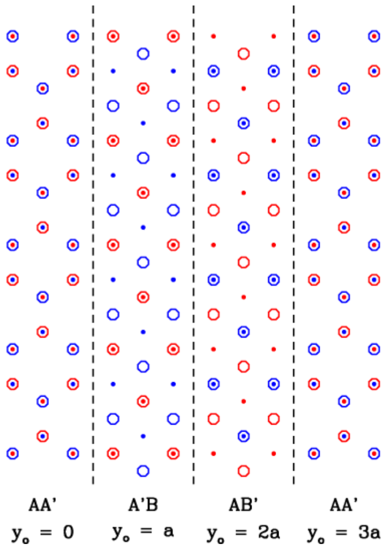

FIG. 20. Stacking for hBN/hBN1.

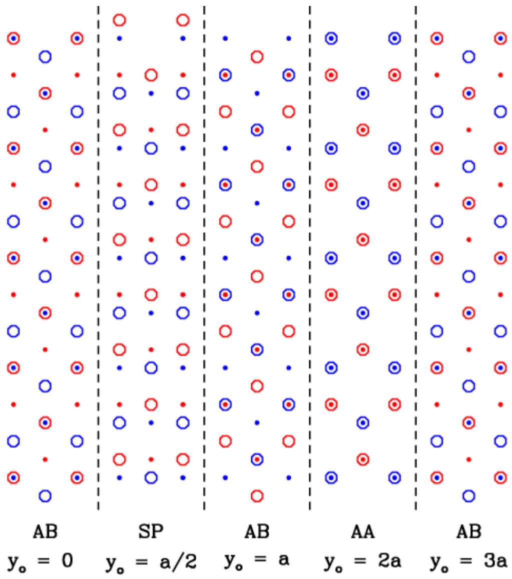

FIG. 21. Stacking for hBN/hBN2.

the free energy per unit area is

$$\frac{\Delta F_{\Delta h}}{Aa_2} = \frac{8\Delta^2\phi^4}{\sqrt{3}}\left(\left(\cos\left(\frac{y_0}{2}\right)-1\right)\sum_{i=1}^{3} f_i \cos\left(\frac{y_0}{2}\right)^i\right), \tag{57}$$

where $\Delta F_{\Delta h} \equiv F_{\Delta h}(y_0) - F_{\Delta h}(0)$,

$$\begin{aligned} f_0 &= \frac{1}{2}\Big[\frac{\sqrt{3}}{4}\big(\alpha_{\rm t}(1+2\Delta\alpha)+11\Delta\alpha^2\big) \\ &\quad -9\Delta\alpha\Delta\alpha_{\rm AB}\sin\frac{y_0}{2}\Big]; \\ f_1 &= 3\Delta\alpha_{\rm AB}\Delta\alpha\sin\frac{y_0}{2} + \sqrt{3}\Big[\alpha_{\rm t}(1+\Delta\alpha) \\ &\quad +\frac{5}{4}\Delta\alpha^2 - \frac{9}{4}\Delta\alpha_{\rm AB}^2\Big]; \\ f_2 &= 3\Delta\alpha_{\rm AB}\Delta\alpha\sin\frac{y_0}{2} + \sqrt{3}\Big[\alpha_{\rm t}(1+\Delta\alpha) \\ &\quad -\frac{1}{2}\Delta\alpha^2 - \frac{3}{2}\Delta\alpha_{\rm AB}^2\Big]; \\ f_3 &= \frac{\sqrt{3}}{2}\Big(3\Delta\alpha_{\rm AB}^2 - \Delta\alpha^2\Big). \end{aligned} \tag{58}$$

and $\alpha_{\rm t} \equiv \alpha_{\rm AA} + \alpha_{\rm BB} + \alpha_{\rm AB}$.

In the hBN/hBN2 configuration the minimum layer spacing is

$$\begin{aligned} \Delta h_{\rm eq} &= \Delta\Big(1 + 2\phi^2\left[\Delta\alpha + \alpha_{\rm t}\right]\big[\cos(y_0/2)(1+\cos(y_0/2)) \\ &\quad -1/2\big]\Big), \end{aligned} \tag{59}$$

with corresponding free energy

$$\begin{aligned} \frac{\Delta F_{\Delta h}}{Aa_2} &= 2\Delta^2\phi^4\Big(4(\Delta\alpha^2 + 3\Delta\alpha_{\rm AB})\cos\frac{y_0}{2} \\ &\quad +\alpha_{\rm t}(\alpha_{\rm t}+2\Delta\alpha) - 3\Delta\alpha^2 - 12\Delta\alpha_{\rm AB}^2\Big) \\ &\quad \left(\cos\frac{y_0}{2} + \frac{1}{2}\right)^2. \end{aligned} \tag{60}$$

Matching Δh for the hBN/hBN1 case at $y_0 = 0, a$ and $2a$ gives

$$\alpha_{\rm AA} = 0.12986,\ \alpha_{\rm BB} = 0.29411,\ \Delta = 3.44\text{Å} \tag{61}$$

$\alpha_{\rm AB}$ was then chosen to provide the best match for the hBN/hBN2 case and is given by

$$\alpha_{\rm AB} = 0.055. \tag{62}$$

The fits shown in Fig. 22 are reasonable good. One could also fit differently e.g. by fitting two points to the hBN/hBN1 and two points to the hBN/hBN2 stackings.

The same procedure to obtain a_2 outlined in the previous section can be used here using the data given in Zhou *et al.* [1] table II for the ACFD-RPA, i.e., d_0 = 3.34 Å, $C_{\rm nn}$ = 46 GPa, $\gamma_{\rm coh}$ = 222.7

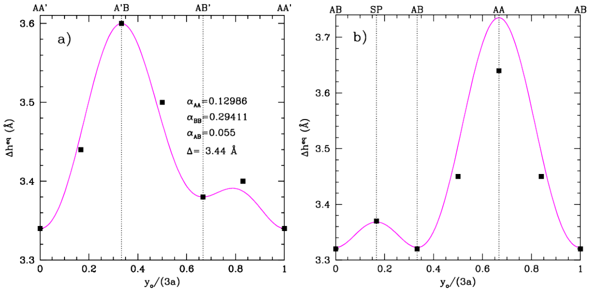

FIG. 22. Equilibrium height as a function of stacking location for a) hBN/hBN1 and b) hBN/HBN2 bilayers.

mJ/m^2. This results in the fit shown in Fig. 23 which gives

$$a_2 = 0.689 \text{ mJ}/(\text{m}^2\text{Å}^2) = 0.430 \text{ eV}/\text{nm}^4, \quad (63)$$

or in dimensionless units,

$$a_{2\text{d}} = 1.01 \times 10^{-4}. \quad (64)$$

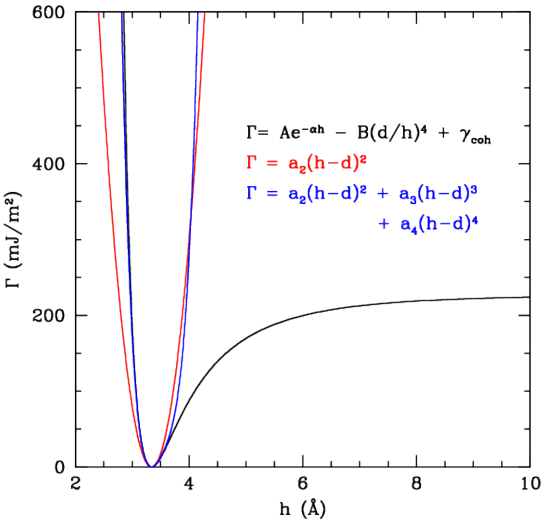

FIG. 23. Fitting the height potential to polynomial for a hBN/hBN bilayer.

The stacking energy for the hBN/hBN bilayer can be written as

$$F_{\text{st}} = \int d\vec{r}\Big(V_{\text{AA}}\delta n_{\text{A}1}\delta n_{\text{A}2} + V_{\text{BB}}\delta n_{\text{B}1}\delta n_{\text{B}2} + \frac{1}{2}V_{\text{AB}}(\delta n_{\text{A}1}\delta n_{\text{B}2} + \delta n_{\text{B}1}\delta n_{\text{A}2}\Big), \quad (65)$$

where the parameters V_{AA}, V_{BB} and V_{AB} must be matched to experiment or theory. Using the mode expansions described in App. D gives for the hBN/hBN1 system

$$\Delta F_{\text{st}}/A = 2\phi^2\left(1-\cos(y_0/2)\right)\left(\cos(y_0/2)[\Delta V + 2] + \sqrt{3}\Delta V_{\text{AB}}\sin(y_0/2)\right), \quad (66)$$

where $\Delta F_{\text{st}} \equiv F_{\text{st}}(y_0) - F_{\text{st}}(y_0 = 0)$,

$$\Delta V \equiv V_{\text{AA}} + V_{\text{BB}} - 2V_{\text{AB}};$$
$$\Delta V_{\text{AB}} \equiv V_{\text{AA}} - V_{\text{BB}}. \quad (67)$$

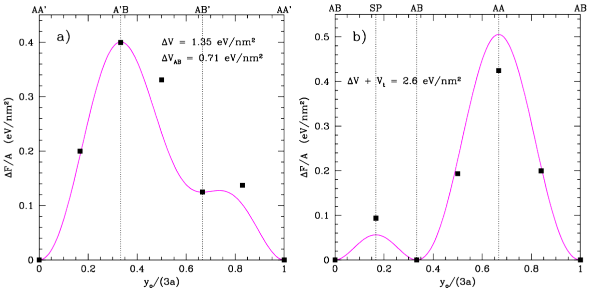

FIG. 24. Stacking energy for a) hBN/hBN1 and b) hBN/hBN2, where the line is from Eq. (66) and the points are from Zhou *et al.* [1]

In the hBN/hBN2 configuration as shown in Fig. 21, the free energy becomes,

$$\Delta F_{\text{st}}/A = \phi^2(\Delta V + V_{\text{t}})\left[2\cos(y_0/2 + a)^2 + 1)\right]^2 \quad (68)$$

where $V_{\text{t}} = V_{\text{AA}} + V_{\text{BB}} + V_{\text{AB}}$. Fitting to the points A'B, AB' for the hBN/hBN1 and AB for the hBN/hBN2 gives

$$\Delta V = V_{\text{AA}} + V_{\text{BB}} - 2V_{\text{AB}} = 1.35 \text{ eV}/\text{nm}^2;$$
$$\Delta V_{\text{AB}} = V_{\text{AA}} - V_{\text{BB}} = 0.71 \text{ eV}/\text{nm}^2;$$
$$V_{\text{t}} + \Delta V = 2.6 \text{ eV}/\text{nm}^2. \quad (69)$$

This gives

$$V_{\text{AA}} = 0.997 \text{ eV}/\text{nm}^2;$$
$$V_{\text{BB}} = 0.287 \text{ eV}/\text{nm}^2;$$
$$V_{\text{AB}} = -0.033 \text{ eV}/\text{nm}^2. \quad (70)$$

In dimensionless units

$$V_{\text{IJd}} = \frac{V_{\text{IJ}}}{c_h}\left(\frac{a_{\text{hBN}}}{a_x}\right)^2 \quad (71)$$

Quantity	Dimensional	Dimensionless
V_{AA}	$0.997\ \mathrm{eV/nm}^2$	4.39×10^{-4}
V_{BB}	$0.287\ \mathrm{eV/nm}^2$	1.21×10^{-4}
V_{AB}	$-0.033\ \mathrm{eV/nm}^2$	-1.46×10^{-5}
a_2	$0.430\ \mathrm{eV/nm}^4$	1.01×10^{-4}
Δ	3.44 Å	9.11
α_{AA}	–	0.130
α_{BB}	–	0.294
α_{AB}	–	0.055

TABLE II. Summary of model parameters hBN/hBN bilayer.

where $c_h = 2.74$ eV, $a_{\mathrm{hBN}} = .251$ nm and $a_x = 4\pi/\sqrt{3}$, which gives relative small values as

$$\begin{aligned} V_{\mathrm{AAd}} &= 4.39 \times 10^{-4}; \\ V_{\mathrm{BBd}} &= 1.21 \times 10^{-4}; \\ V_{\mathrm{ABd}} &= -0.146 \times 10^{-4}. \end{aligned} \tag{72}$$

The fits are shown in Fig. 24 and a summary of the parameters is given in Table II.

C. Monatomic/binary bilayer (graphene/hBN)

Similar calculations can be performed for a graphene/hBN system (ignoring the lattice constant difference). The stacking sequence is shown in Fig. 25. For a graphene/hBN bilayer Δh can be written as

$$\Delta h^0 = \Delta(1 + \alpha_{\mathrm{gA}}\delta n_{\mathrm{g}}\delta n_{\mathrm{A}} + \alpha_{\mathrm{gB}}\delta n_{\mathrm{g}}\delta n_{\mathrm{B}}). \tag{73}$$

Integrating over a unit cell and minimizing w.r.t. Δh gives

$$\begin{aligned} \frac{\Delta h^{\mathrm{eq}}}{\Delta} = 1 - \frac{2\phi_{\mathrm{g}}\phi_h}{\sqrt{3}}\big[&\sqrt{3}\alpha_{\mathrm{t}}\cos(y_0/2)(1+\cos(y_0/2)) \\ &-3\Delta\alpha\sin(y_0/2)(\cos(y_0/2)-1) - \sqrt{3}\alpha_{\mathrm{t}}/2\big], \end{aligned} \tag{74}$$

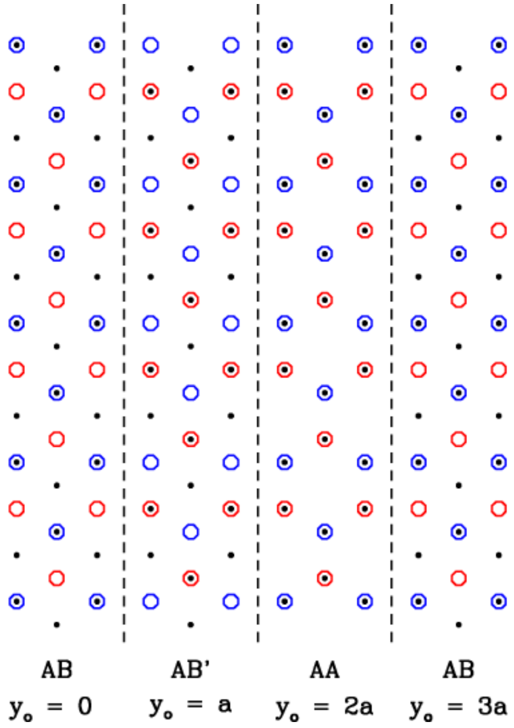

FIG. 25. stacking for graphene/hBN

with energy density

$$\begin{aligned} \frac{\Delta F_{\Delta h}}{Aa_2} = \frac{32\phi_{\mathrm{g}}^2\phi_h^2\Delta^2}{\sqrt{3}}\Big[&\sqrt{3}(\alpha_{\mathrm{A}}^2 - \alpha_{\mathrm{A}}\alpha_{\mathrm{B}} + \alpha_{\mathrm{B}}^2)\cos^3\frac{y_0}{2} \\ &-\frac{\sqrt{3}}{8}(\alpha_{\mathrm{A}}^2 - 4\alpha_{\mathrm{A}}\alpha_{\mathrm{B}} + \alpha_{\mathrm{B}}^2)\cos^2\frac{y_0}{2} \\ &-\frac{\sqrt{3}}{8}(7\alpha_{\mathrm{A}}^2 - 10\alpha_{\mathrm{A}}\alpha_{\mathrm{B}} + 7\alpha_{\mathrm{B}}^2)\cos\frac{y_0}{2} \\ &+\frac{3}{8}\left(\alpha_{\mathrm{A}}^2 - \alpha_{\mathrm{B}}^2\right)\sin\frac{y_0}{2}\left(\cos\frac{y_0}{2} - 1\right) \\ &+\frac{3\sqrt{3}}{16}\alpha_{\mathrm{B}}(2\alpha_{\mathrm{A}} - 3\alpha_{\mathrm{B}})\Big]. \end{aligned} \tag{75}$$

Matching this to Zhou *et al.* [1] gives, gives $\Delta = 3.45$ Å and $\alpha_{\mathrm{A}} = 0.0370$ and $\alpha_{\mathrm{B}} = 0.195$. This fit is very good as shown in Fig. 26.

The coefficient a_2 can be calculated similar to the prior cases to obtain

$$\begin{aligned} a_2 &= 0.497\ \mathrm{mJ/(m^2Å^2)} = 0.310\ \mathrm{eV/nm}^4; \\ a_{2d} &= 7.31 \times 10^{-5}, \end{aligned} \tag{76}$$

where the fits are shown in Fig. 27.

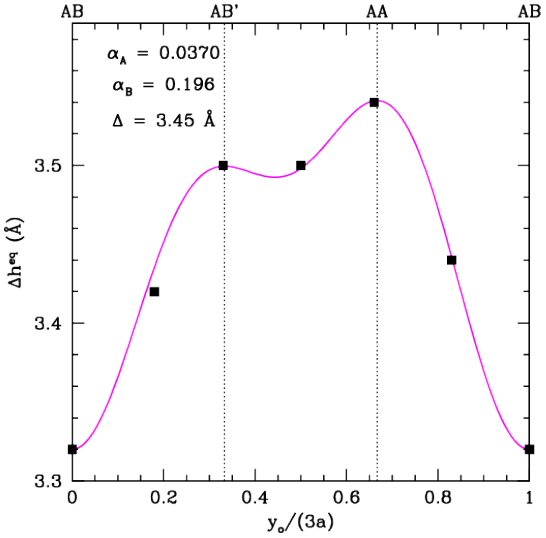

FIG. 26. Equilibrium height as a function of stacking location for graphene/hBN bilayer.

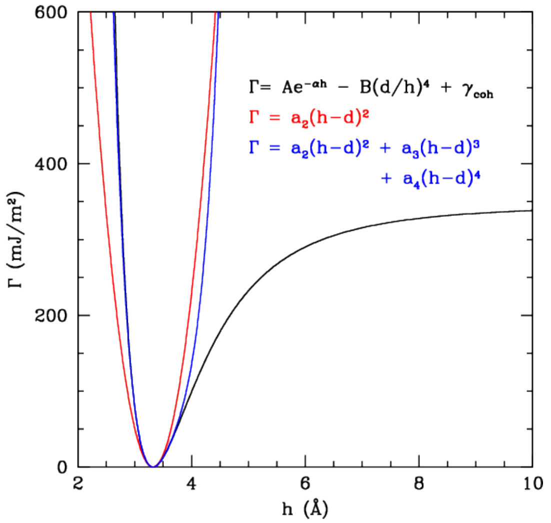

FIG. 27. Fitting height potential to a polynomial for graphene/hBN bilayer.

For this system a coupling term,

$$F_{\rm st} = \int d\vec{r}\,(V_{\rm A}\delta n_{\rm A} + V_{\rm B}\delta n_{\rm B})\,\delta n_{\rm g} \tag{77}$$

Quantity	Dimensional	Dimensionless
$V_{\rm A}$	0.145 eV/nm^2	2.64×10^{-5}
$V_{\rm B}$	1.135 eV/nm^2	2.06×10^{-4}
a_2	0.310 eV/nm^4	7.31×10^{-5}
Δ	3.45 Å	9.78
$\alpha_{\rm A}$	–	0.037
$\alpha_{\rm B}$	–	0.196

TABLE III. Summary of model parameters graphene/hBN bilayer.

leads to a stacking energy

$$\begin{aligned}\frac{\Delta F_{\rm st}}{A} = -2\phi_{\rm g}\phi_{\rm AB}\Big[&V_{\rm T}\cos\frac{y_0}{2}\left(1+\cos\frac{y_0}{2}\right)\\ &-\Delta V\sqrt{3}\sin\frac{y_0}{2}\left(\cos\frac{y_0}{2}-1\right)\\ &-\left(2V_{\rm A}-\frac{5}{2}V_{\rm B}\right)\Big]\end{aligned} \tag{78}$$

where $V_{\rm T} = V + {\rm A} + V_{\rm B}$ and $\Delta V = V_{\rm A} - V_{\rm B}$. The best fit shown in Fig. 28 is very good and occurs for

$$\begin{aligned}V_{\rm A} &= 0.145\ {\rm eV/nm^2};\\ V_{\rm B} &= 1.135\ {\rm eV/nm^2}.\end{aligned} \tag{79}$$

To convert to dimensionless form one has to choose either graphene or hBN parameters for the energy scale ($c_{\rm g} = 6.58$ eV/nm^2, $c_h = 2.74$ eV/nm^2) and the lattice spacing ($a_{\rm g} = 2.56$ Å, $a_h = 2.51$ Å). If graphene parameters are chosen

$$\begin{aligned}V_{\rm Ad} &= 2.64 \times 10^{-5};\\ V_{\rm Bd} &= 2.06 \times 10^{-4}.\end{aligned} \tag{80}$$

It should be noted that for this system in dimensionless form the hBN free energy would need to be multiplied by $c_h/c_{\rm g}$ and the $(1+\nabla^2)$ would need to be modified in the hBN free energy to account for the difference in length scales, i.e., it would become $((a_{\rm g}/a_h)^2+\nabla^2)$. A summary of parameters is given in Table III.

IV. SUMMARY AND CONCLUSIONS

The model phase-field crystal model presented in Sec. II (i.e., Eqs. (4)-(6)) here provides a relatively simple method of modeling small out of plane deformations (OPDs) in a single atomic layer and naturally incorporates elastic and plastic deformations

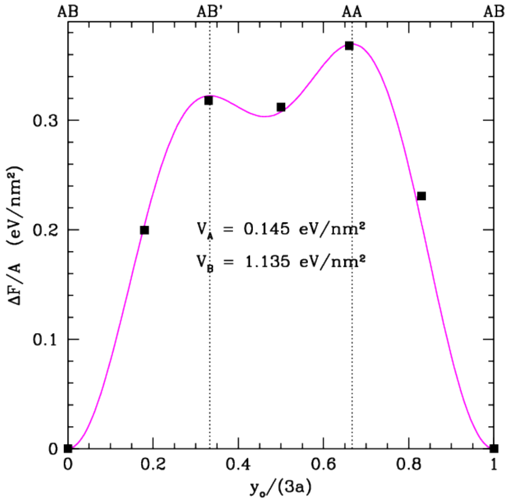

FIG. 28. Stacking energy for graphene/hBN, where the line is from Eq. (66) and the points are from Zhou *et al.* [1]

within the plane. This model was validated in the small deformation limit, by showing it reduces to a standard model used for flexible sheets. Sample simulations of strained sheets were shown to be consistent with analytic expressions derived from continuum theory for the height of the induced deformations as well as the associated excess free energy to further valid the model and simulation technique. The flexibility of the model was illustrated by applications to dislocation dipoles and grain boundary energies in graphene. In former case, in the absence of OPDs, the model was again shown to be consistent with continuum elasticity theory for the strain fields due to point dislocations. Allowing for OPDs made a large impact on reducing the energy of the dislocation pairs and removed the logarithmic divergence of the pair energy with system size, consistent with expectations of other publications [39, 59]. In addition the predicted energy of a 5/7 dislocation was quantitatively consistent with prior DFT calculations [30, 59, 65, 66]. Simulations of grain boundaries also showed how the OPDs lead to a lowering of the grain boundary energies in a manner qualitatively consistent with prior MD simulations [27], although the decreases were smaller than the low temperature MD simulations.

In Sec. III the construction of a continuum model of stacked 2D layers was developed using an assumption that variations in the distance between layers did not vary greatly. With a relatively simple coupling it was shown that the model could be parameterized to match the stacking energies and heights of prior DFT calculations quite closely. This was shown in three separate bilayers, graphene/graphene, hBN/hBN and graphene/hBN. The approach taken was similar but somewhat different than the approach of Zhou *et al.* [1] in which a continuum model is developed in that it contained a much smaller parameter set and was able to fit to the DFT model deemed the most accurate. Sample simulations of twisted bilayers of graphene were shown to reproduce the breathing mode observed by Zhou *et al.* [1], although an extensive study was not undertaken to see if the model could also reproduce the twisted mode reported by these researchers (it should be noted that strain induced similar twisted modes have been reproduced in other PFC studies [69, 70]). Additionally a study of domain walls created by an AB/BA boundary in one layer are shown to be consistent with prior research of Alden *et al.* [68]. Finally the ability of the model to incorporate complex microstructures that include dislocation and grain boundaries, was illustrated by examining the influence of a grain boundary or polycrystalline layer on an adjacent undefected layer.

Overall the model proposed here is perhaps the simplest one for stacks of flexible sheets that incorporates OPDs as well as in-plane deformations and dislocations that can be parameterized by matching to known results. The simplicity of the model facilitates relatively low-overhead numerical calculations, but limits the applicability to relatively small deformations. In each layer a Monge gauge was assumed that limits the model to small OPDs and thus cannot handle multi-valued heights. Similarly, the multiple layer model assumes that deviations from the equilibrium distance between two layers are small such that the stacking interaction potential (Γ) can approximated by a simple polynomial. This approximation implies that an unphysical infinite energy would be required to pull the bilayers apart. It should be possible to implement a more accurate form (i.e., 45) if needed.

It was shown that by adding more bulk coupling terms (eg., terms of the form $\delta n_1^i \delta n_2^j$, where i and j are integers) more complex stacking energies and heights could be fit quite accurately. However, as shown in Sec. III A, using the one-mode approximation for the density field will not lead to accurate parameterization for the full model, and thus the parameters should be chosen numerically. In this regard it would be extremely useful to develop an complex amplitude expansion of the model as has been done for the basic PFC case [50–54] and more complex systems [55, 63]. In this approach the one-mode approximation is exact making parameter fitting easier in addition to the fact that the approach can be used to computationally study even larger system sizes.

V. ACKNOWLEDGEMENTS

K. R. E. acknowledges support from the National Science Foundation under Grant No. DMR-1506634 and Oakland Unversity Technology Services and high-performance research computing facility (Matilda). The authors acknowledges useful discussions with Petri Hirvonen, Zheyong Fan, Axel Voigt, Zhi-Feng Huang and Marco Salvalaglio. E. G. was supported by Fundação de Amparo à Pesquisa do Estado de São Paulo - FAPESP (Grant No. 18/19586-9). This work has also been supported in part by the Academy of Finland though its QTF Center of Excellence grant no. 312298.

Appendix A: Laplacian and Curvature in the Monge Gauge

Consider a two-dimensional sheet in the (x, y) plane embedded in three dimensional space with height $h(x, y)$. It will be assumed that h is a single-valued function of (x, y), i.e., a Monge gauge will be used. This limits the approach to small out of plane deformations. Transforming from $\vec{r} = (x, y, z)$ coordinates to $\vec{w} = (x, y, h(x, y))$ is straightforward and leads to the transformation matrix $\mathbf{A}$ (with components $A_{ij} = \partial w_i/\partial r_j$) of the form,

$$\mathbf{A} = \begin{pmatrix} 1 & 0 & h_x \\ 0 & 1 & h_y \\ 0 & 0 & 0 \end{pmatrix}, \tag{A1}$$

where $h_i \equiv \partial_i h$. From A the metric $\mathbf{G}$ (with elements $g_{ij} = a_{ki}a_{kj}$) can be constructed, i.e.,

$$\mathbf{G} = \begin{pmatrix} 1 + h_x^2 & h_x h_y \\ h_x h_y & 1 + h_y^2 \end{pmatrix}. \tag{A2}$$

The inverse of this metric is then,

$$\mathbf{G}^{-1} = \frac{1}{1 + h_x^2 + h_y^2} \begin{pmatrix} 1 + h_y^2 & -h_x h_y \\ -h_x h_y & 1 + h_x^2 \end{pmatrix}. \tag{A3}$$

The Laplacian can now be written in terms of the elements of the inverse matrix g^{ij} and the determinant of the Jacobian of the transformation ($J = \sqrt{|\mathbf{G}|} = \sqrt{1 + |\vec{\nabla} h|^2}$), i.e.,

$$\nabla_w^2 = \frac{1}{J} \sum_{ij} \partial_i \left(J g^{ij} \partial_j \right). \tag{A4}$$

This gives

$$\nabla_w^2 = \frac{1}{J} \left[\partial_x \left(\frac{1 + h_y^2}{J} \partial_x \right) + \partial_y \left(\frac{1 + h_x^2}{J} \partial_y \right) \right. \\ \left. - \partial_x \left(\frac{h_x h_y}{J} \partial_y \right) - \partial_y \left(\frac{h_x h_y}{J} \partial_x \right) \right]. \tag{A5}$$

In this limit that gradients in h are small this simplified to lowest order,

$$\nabla_w^2 \approx \nabla_{xy}^2 - (h_x^2 \partial_x^2 + h_y^2 \partial_y^2 + 2 h_x h_y \partial_x \partial_y). \tag{A6}$$

Appendix B: Functional Derivatives

The functional derivative with respect to n of the free energy described in Eq. (13) is

$$\frac{\delta F}{\delta n} = \Delta B n + \tau n^2 + v n^3 + \left[1 + \partial_x^2 \left(1 - h_x^2 \right) \right. \\ \left. + \partial_y^2 \left(1 - h_y^2 \right) - 2 \partial_x \partial_y h_x h_y \right] (1 + \nabla_w^2) n,$$

where the derivatives operate on any function to the right. Similarly with respect to h gives,

$$\frac{\delta F}{\delta h} = \kappa C * h + 2 \left[\partial_x \left(h_x n_{xx} + h_y n_{xy} \right) + \right. \\ \left. \partial_y \left(h_y n_{yy} + h_x n_{xy} \right) \right] (1 + \nabla_w^2) n,$$

where the ∂_x and ∂_y operators act on all quantities to the right and

$$C * h \equiv \int d\vec{r}' C(|\vec{r} - \vec{r}'|) h(\vec{r}'). \tag{B1}$$

Letting $L = 1 + \nabla^2$ and $H = h_x^2 \partial_{xx} + h_y^2 \partial_{yy} + 2 h_x h_y \partial_{xy}$ gives,

$$\frac{\delta F}{\delta n} = \Delta B n + \tau n^2 + v n^3 + L^2 n \\ - \partial_x^2 (h_x^2 (1 + \nabla_w^2) n + H n) \\ - \partial_y^2 (h_y^2 (1 + \nabla_w^2) n + H n) \\ - 2 \partial_x \partial_y h_x h_y (1 + \nabla_w^2) n - H n. \tag{B2}$$

Appendix C: Strain Calculations

As discussed in Refs. [60–62] for the original PFC model, the strain can be calculated from a free energy functional via the expression,

$$\sigma^n_{ik} = \partial_j \left[\frac{\partial f}{\partial(\partial_{ij} n)} \partial_k n \right] - \frac{\partial f}{\partial(\partial_{ij} n)} \partial_{kj} n,$$

where f is the integrand of the free energy functional. For the free energy used in this manuscript,

$$\frac{\partial f}{\partial(\partial_{xx} n)} = (1 - h_x^2)\mathcal{L}_h n; \tag{C1}$$

$$\frac{\partial f}{\partial(\partial_{yy} n)} = (1 - h_y^2)\mathcal{L}_h n; \tag{C2}$$

$$\frac{\partial f}{\partial(\partial_{xy} n)} = -2 h_x h_y \mathcal{L}_h n. \tag{C3}$$

This gives rise to the following expressions for the strains:

$$\sigma^n_{xx} = \left(\partial_x \left[(1 - h_x^2)\mathcal{L}_h n\right] - 2\partial_y \left[h_x h_y \mathcal{L}_h n\right]\right) \partial_x n - \left[(1 - h_x^2)\mathcal{L}_h n\right] \partial_{xx} n + \left[2 h_x h_y \mathcal{L}_h n\right] \partial_{xy} n; \tag{C4}$$

$$\sigma^n_{yy} = \left(\partial_y \left[(1 - h_y^2)\mathcal{L}_h n\right] - 2\partial_x \left[h_x h_y \mathcal{L}_h n\right]\right) \partial_y n - \left[(1 - h_y^2)\mathcal{L}_h n\right] \partial_{yy} n + \left[2 h_x h_y \mathcal{L}_h n\right] \partial_{xy} n; \tag{C5}$$

$$\sigma^n_{xy} = \left(\partial_x \left[(1 - h_x^2)\mathcal{L}_h n\right] - 2\partial_y \left[h_x h_y \mathcal{L}_h n\right]\right) \partial_y n - \left[(1 - h_x^2)\mathcal{L}_h\right] \partial_{xy} n + \left[2 h_x h_y \mathcal{L}_h n\right] \partial_{yy} n; \tag{C6}$$

$$\sigma^n_{yx} = \left(\partial_y \left[(1 - h_y^2)\mathcal{L}_h n\right] - 2\partial_x \left[h_x h_y \mathcal{L}_h n\right]\right) \partial_x n - \left[(1 - h_y^2)\mathcal{L}_h\right] \partial_{xy} n + \left[2 h_x h_y \mathcal{L}_h n\right] \partial_{xx} n. \tag{C7}$$

These calculations lead to strains that vary on short length scales. To make a comparison with the continuum model the strains obtain were filtered in Fourier spaces to obtain smooth strains, σ_{ij}, i.e., in Fourier space,

$$\sigma_{ij}(\vec{k}) = \int d\vec{k}\, e^{-ak^2} \sigma^n_{ij}(\vec{k}) \tag{C8}$$

where a determines the magnitude of smoothing. Choosing a is a trade-off as too large a value will smooth out the dislocation core and too small a value will lead to spurious fluctuations in the bulk regions. σ_{xx} is shown in Fig. 29 for $a = 5, 7$ and 9. Clearly at $a = 5$ there are very evident spurious fluctuations, but by $a = 7$ they are quite small and gone by $a = 9$. However, as can be seen there is significant reductions near the center of the dislocation core as a as increased. For comparisons given in this paper a value of $a = 7$ was chosen as the best compromise.

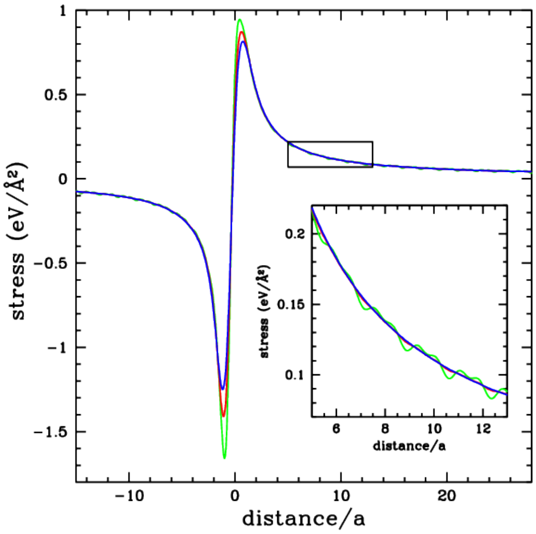

FIG. 29. Comparison of simulated stress σ_{xx} for different values of the smoothing parameter a given in Eq. (C8). The green, red and blue lines correspond to $a = 5, 7$ and 9 respectively.

Appendix D: Hexagonal Boron Nitride model

The free energy functional can be written [28, 29],

$$\frac{F}{c_h} = \int d\vec{r} \Big[-\frac{\varepsilon_A}{2} n_A^2 + \frac{1}{2}\left((\nabla^2 + q_A^2) n_A\right)^2 - \frac{g_A}{3} n_A^3 + \frac{1}{4} n_A^4 - \frac{\varepsilon_B}{2} n_B^2 + \frac{\beta_B}{2}\left((\nabla^2 + q_B^2) n_B\right)^2 - \frac{g_B}{3} n_B^3 + \frac{v}{4} n_B^4 + \alpha_{AB} n_A n_B + \frac{w}{2} n_A^2 n_B + \frac{u}{2} n_A n_B^2 \Big] \tag{D1}$$

with parameters $\varepsilon_A = \varepsilon_B = 0.3$, $q_A = q_B = 1$, $\alpha_{AB} = 0.5$, $g_A = g_B = 0.5$, $w = u = 0.3$, $\beta_B = v = 1$

and $c_h = 2.74$ eV. The lattice constant in hBN is $a_x = 2.51$ Å. With these parameters the model is symmetric (if the average densities are the same) and the one mode approximation can be written,

$$\begin{aligned} n_{\mathrm{A}} &= n_0 + 2\phi\left(2\cos\left(\frac{\sqrt{3}}{2}x\right)\cos\Big(\frac{y}{2}\Big) + \cos(y)\right) \\ n_{\mathrm{B}} &= n_0 + 2\phi\Bigg(2\cos\left(\frac{\sqrt{3}}{2}x\right)\cos\Big(\frac{y}{2} + 2\pi/3\Big) \\ &\qquad + \cos(y + 4\pi/3)\Big)\Bigg) \end{aligned} \tag{D2}$$

where $n_0 = -0.28$. Minimizing the free energy with respect to ϕ gives

$$\begin{aligned} \phi = \Big(&6g - 12n_0 + 3u + \big(3(12g(g+u) + 192n_0(g-n_0) \\ &+u(3u - 24n_0) + 40\alpha_{\mathrm{AB}} + 80\varepsilon)\big)^{1/2}\Big)/60 \end{aligned} \tag{D3}$$

[1] S. Zhuo, J. Han, S. Dai, J. Sun, and D. J. Srolovitz, Phys. Rev. B **92**, 155438 (2015).

[2] S. Z. Butler, S. M. Hollen, L. Cao, J. A. Cui, Y. Gupta, H. R. R. Gutiérrez, T. F. Heinz, S. S. Hong, J. Huang, A. F. Ismach, E. Johnston-Halperin, M. Kuno, V. V. Plashnitsa, R. D. Robinson, S. Ruoff, R. S. Salahuddin, J. Shan, L. Shi, M. G. Spencer, M. Terrones, W. Windl, and J. E. Goldberger, ACS Nano **7**, 2898 (2013).

[3] G. R. Bhimanapati, Z. Lin, V. Meunier, Y. Jung, J. Cha, S. Das, D. Xiao, Y. Son, M. S. Strano, V. R. Cooper, L. Liang, S. G. Louie, E. Ringe, W. Zhou, S. S. Kim, R. R. Naik, B. G. Sumpter, H. Terrones, F. Xia, Y. Wang, J. Zhu, D. Akinwande, N. Alem, J. A. Schuller, R. E. Schaak, M. Terrones, and J. A. Robinson, ACS Nano **9**, 11509 (2015).

[4] F. H. L. Koppens, T. Mueller, P. Avouris, M. S. Vitiello, and M. Polini, Nature Nanotechnology **9**, 780 (2014).

[5] F. Xia, H. Wang, D. Xiao, M. Dubey, and A. Ramasubramaniam, Nature Photonics **8**, 899 (2014).

[6] D. Deng, K. S. Novoselov, Q. Fu, N. Zheng, N. Tian, and X. Bao, Nature Nanotechnology **11**, 218 (2016).

[7] M. Bernardi, M. Palummo, and J. C. Grossman, Nano Lett. **13**, 3664 (2013).

[8] G. Herzer, Acta Mater. **61**, 718 (2013).

[9] C. H. Chen, S. Kodat, M. H. Walmer, S.-F. Chen, M. A. Willard, and V. G. Harris, J. App. Phys. **93**, 7966 (2003).

[10] S. Roy, I. Dubenko, D. D. Edorh, and N. Ali, J. App. Phys. **96**, 1202 (2004).

[11] D. Xue, G. Chai, X. Li, and X. Fan, J. Mag. Mag. Mat. **320**, 1541 (2008).

[12] S. Yip, Nature **391**, 532 (1998).

[13] E. O. Hall, Proc. Phys. Soc. London, Sect. B **64**, 747 (1951).

[14] N. J. Petch, J. Iron Steel Inst., London **174**, 25 (1953).

[15] A. Cracknell and N. Petch, Acta Metall. **3**, 186 (1955).

[16] K. Lu, W. Wei, and J. Wang, Scr. Metall. Mater. **24**, 2319 (1990).

[17] A. Chokshi, A. Rosen, J. Karch, and H. Gleiter, Scr. Metall. **23**, 1679 (1989).

[18] Z. Fan, L. Felipe, C. Pereira, P. Hirvonen, M. M. Ervasti, K. R. Elder, D. Donadio, T. Ala-Nissila, and A. Harju, Phys. Rev. B **95**, 144309 (2017).

[19] Z. Fan, P. Hirvonen, L. F. C. Pereira, M. M. Ervasti, K. R. Elder, D. Donadio, A. Harju, and T. Ala-Nissila, Nano Lett. **17**, 5919 (2017).

[20] K. Azizi, P. Hirvonen, Z. Fan, A. Harju, K. R. Elder, T. Ala-Nissila, and S. M. V. Allaei, Carbon **125**, 384 (2017).

[21] H. K. Dong, P. Hirvonen, Z. Y. Fan, and T. Ala-Nissila, Phys. Chem. Chem. Phys. **20**, 24602 (2018).

[22] W. Zhou, X. Zou, S. Najmaei, Z. Liu, Y. Shi, J. Kong, J. Lou, P. M. Ajayan, B. I. Yakobson, and J.-C. Idrobo, Nano Lett. **13**, 2615 (2013).

[23] A. M. van der Zande, P. Y. Huang, D. A. Chenet, T. C. Berkelbach, Y. You, G.-H. Lee, T. F. Heinz, D. R. Reichman, D. A. Muller, and J. C. Hone, Nat. Mater. **12**, 554 (2013).

[24] K. R. Elder, M. Katakowski, M. Haataja, and M. Grant, Physical Review Letters **88**, 245701 (2002).

[25] K. R. Elder and M. Grant, Phys. Rev. E **70**, 051605 (2004).

[26] K. R. Elder, N. Provatas, J. Berry, P. Stefanovic, and M. Grant, Phys. Rev. B **75**, 064107 (2007).

[27] P. Hirvonen, M. M. Ervasti, Z. Fan, M. Jalalvand, M. Seymour, S. M. V. Allaei, N. Provatas, A. Harju, K. R. Elder, and T. Ala-Nissila, Phys. Rev. B **94**, 035414 (2016).

[28] D. Taha, S. K. Mkhonta, K. R. Elder, and Z.-F. Huang, Phys. Rev. Lett. **118**, 255501 (2017).

[29] D. Taha, S. R. Dlamini, S. K. Mkhonta, K. R. Elder, and Z.-F. Huang, Phys. Rev. Mat. **3**, 095603 (2019).

[30] O. V. Yazyev and S. G. Louie, Phys. Rev. B **81**, 195420 (2010).

[31] J. da Silva Araújo and R. W. Nunes, Phys. Rev. B **81**, 073408 (2010).

[32] P. Hirvonen, Z. Fan, M. M. Ervasti, A. Harju, K. R. Elder, and T. Ala-Nissila, Sci. Rep. **7**, 4754 (2017).

[33] J. Li, B. Ni, T. Zhang, and H. Gao, J. Mech. Phys. Solids **120**, 36 (2018).

[34] C. M. Funkhouser, F. J. Solis, and K. Thornton, Phys. Rev E **76**, 011912 (2007).

[35] C. M. Funkhouser, M. Mayer, M. F. J. Solis, and K. Thornton, J. Chem. Phys. **138**, 024909 (2013).

[36] S. Aland, A. Rätz, M. Röger, and A. Voigt, Multiscale Model. Simul. **10**, 82 (2012).

[37] R. Backofen, A. Voigt, and T. Witkowski, Phys. Rev. E **81**, 025701 (2010).

[38] D. R. Nelson and L. Peliti, Journal de Physique **48**, 1085 (1987).

[39] H. S. Seung and D. R. Nelson, Phys. Rev. A **38**, 1005 (1988).

[40] J. H. Los, M. I. Katsnelson, O. V. Yazyev, K. V. Zakharchenko, and A. Fasolino, Phys. Rev. B **80**, 121405(R) (2009).

[41] J. Swift and P. C. Hohenberg, Phys. Rev. A **15**, 319 (1977).

[42] S. K. Mkhonta, K. R. Elder, and Z.-F. Huang, Phys. Rev. Lett. **111**, 035501 (2013).

[43] S. K. Mkhonta, K. R. Elder, and Z.-F. Huang, Phys. Rev. Lett. **116**, 205502 (2016).

[44] R. Lifshitz and D. M. Petrich, Phys. Rev. Lett. **79**, 1261 (1997).

[45] D. J. Ratliff, A. J. Archer, P. Subramanian, and A. M. Rucklidge, Phys. Rev. Lett. **123**, 148004 (2019).

[46] K.-A. Wu, A. Adland, and A. Karma, Phys. Rev. E **81**, 061601 (2010).

[47] M. Greenwood, N. Provatas, and J. Rottler, Phys. Rev. Lett. **105**, 045702 (2010).

[48] M. Greenwood, J. Rottler, and N. Provatas, Phys. Rev. E **83**, 031601 (2011).

[49] V. W. L. Chan, N. Pisutha-Arnond, and K. Thornton, Phys. Rev. E **91**, 053305 (2015).

[50] N. Goldenfeld, B. P. Athreya, and J. A. Dantzig, Phys. Rev. E **72**, 020601 (2005).

[51] N. Goldenfeld, B. P. Athreya, and J. A. Dantzig, J. Stat. Phys. **125**, 1015 (2006).

[52] B. P. Athreya, N. Goldenfeld, and J. A. Dantzig, Phys. Rev. E **74**, 011601 (2006).

[53] B. P. Athreya, N. Goldenfeld, J. A. Dantzig, M. Greenwood, and N. Provatas, Phys. Rev. E **76**, 056706 (2007).

[54] D.-H. Yeon, Z.-F. Huang, K. Elder, and K. Thornton, Philos. Mag. **90**, 237 (2010).

[55] K. R. Elder, Z.-F. Huang, and N. Provatas, Phys. Rev. E **81**, 011602 (2010).

[56] N. Provatas and K. Elder, *Phase-field methods in materials science and engineering* (John Wiley & Sons, 2011).

[57] P. M. Chaikin and T. C. Lubensky, *Principles of condensed matter physics* (Cambridge University Press, 1995).

[58] S. Dai, Y. Xiang, and D. J. Srolovitz, Nano Lett. **16**, 5923 (2016).

[59] S. Chen and D. C. Chrzan, Phys. Rev. B **84**, 214103 (2011).

[60] A. Skaugen, L. Angheluta, and J. Viñals, Phys. Rev. B **97**, 054113 (2018).

[61] A. Skaugen, L. Angheluta, and J. Viñals, Phys. Rev. Lett. **121**, 255501 (2018).

[62] M. Salvalaglio, L. Angheluta, Z.-F. Huang, A. Voigt, K. R. Elder, and J. Vinals, J. Mech. Sol. **137**, 103865 (2020).

[63] M. Salvalagio, A. Voigt, and K. R. Elder, njp Comp. Mat. **5**, 48 (2019).

[64] D. W. Brenner, O. A. Shenderova, J. A. Harrison, S. J. Stuart, B. Ni, and S. B. Sinnott, J. Phys.: Condens. Matter **14**, 783 (2002).

[65] S. J. Stuart, A. B. Tutein, and J. A. Harrison, J. Chem. Phys. **112**, 6472 (2000).

[66] Y. Liu and B. I. Yakobson, Nano Lett. **10**, 2178 (2010).

[67] S. Tang, H. Wang, Y. Zhang, A. Li, H. Xie, X. Liu, L. Liu, T. Li, F. Huang, X. Xie, and M. Jiang, Sci. Rep. **3**, 2666 (2013).

[68] J. S. Alden, A. W. Tsen, P. Y. Huang, R. Hovden, L. Brown, J. Park, D. A. Muller, and P. L. McEuen, PNAS **110**, 11256 (2013).

[69] K. R. Elder, Z. Chen, K. L. M. Elder, P. Hivonen, S. K. Mkhonta, S.-C. Ying, E. Granato, Z.-F. Huang, and T. Ala-Nissila, J Chem Phys. , 174703 (2016).

[70] K. R. Elder, C. V. Achim, E. Granato, S.-C. Ying, and T. Ala-Nissila, Phys. Rev. B , 195439 (2017).